AN EXPLORATION OF THE GROWTH OF $In_2Se_3/NbSe_2$ HETEROSTRUCTURES

By

Maya Bostock

A THESIS

Submitted to
Michigan State University
in partial fulfillment of the requirements
for the degree of

Physics—Master of Science

2026

ABSTRACT

Ultra-thin film heterostructures are an interesting platform to characterize a wide array of physical phenomena. Engineering vertical and lateral heterostructures allows for the study of the interactions between the chosen materials and the resultant effect on the electronic properties of the system. In_2Se_3 is a highly polymorphic van der Waals material with many different stable phases with an array of electronic properties, including robust ferroelectric phases in the monolayer regime. These properties make it an interesting candidate for heterostructure applications. Using Molecular Beam Epitaxy, $NbSe_2$ and In_2Se_3 are deposited with a sub monolayer coverage to allow for the formation of both vertical and lateral heterostructures. The growth dynamics of the In_2Se_3 film is discussed. Scanning Tunneling Microscopy and Spectroscopy are used to characterize the materials. A Moiré pattern is formed in the vertical heterostructure between the two thin films, the interaction between which stabilizes a partial structure of In_2Se_3 consisting of three out of the five total atomic layers that make up a monolayer. The lateral heterostructures formed directly on the HOPG substrate consist of the full 5-layer In_2Se_3 structure. Preliminary results of the electronic properties of the vertical and lateral heterostructures are presented and future research directions are suggested.

To Grandad

ACKNOWLEDGMENTS

This thesis work was conducted in Prof. Pengpeng Zhang's laboratory with the help co-worker and fellow graduate student Yasemin $\ddot{O}$zbek. I would like to thank Rachel Younger, Paul Gueye, and Remco Zegers, who have supported me through an incredibly difficult transition in my life. Thank you to the National Society of Black Physicists for being an incredible community. Thank you to the friends and family who have supported me throughout this journey, especially Mom and Beau. I also want to thank my cat Ella, who insisted on sitting on or next to me while I wrote most of this thesis. I'm incredibly grateful for my support system and I will continue to make y'all proud.

TABLE OF CONTENTS

LIST OF FIGURES vii

LIST OF ABBREVIATIONS xi

CHAPTER 1 INTRODUCTION 1
1.1 Motivations to Study $In_2Se_3/NbSe_2$ System 1
1.2 Epitaxial Thin Films 2
1.3 Moiré Pattern Background 7
1.4 Lateral Heterostructure Background 8
1.5 In This Thesis 8

CHAPTER 2 EXPERIMENTAL METHODS 9
2.1 Molecular Beam Epitaxy 9
2.2 Scanning Tunneling Microscopy 10

CHAPTER 3 MATERIAL GROWTH AND THE STRUCTURES ON THE SAMPLES 13
3.1 Material Properties 13
3.2 Growth Parameters 17
3.3 Short In_2Se_3 Islands 28
3.4 Tall In_2Se_3 Islands 33

CHAPTER 4 CONCLUSION 41

BIBLIOGRAPHY 42

LIST OF FIGURES

Figure 1.1 WSe_2 Growth on Different Substrates a.) HOPG substrate, b.) graphene/SiC substrate 6

Figure 1.2 Simulated Moiré patterns for hexagonal lattices with either a lattice mismatch or a rotation angle between layers, a.) The substrate and adlayer lattice constants are 3.4Å and 4.0Å, respectively, b.) Both layers have a 3.4Å lattice constant, which a twist angle of 10^o. The code used to create these images was created and refurbished by other graduate students in the group. 7

Figure 1.3 Lateral Heterostructure (left) versus Vertical Heterostructure (right) 8

Figure 3.1 $NbSe_2$ Growth on Different Substrates a.) HOPG substrate, b.) graphene/SiC substrate. Scanning conditions: a.) -2V, 10pA, b.) 2V, 10pA. 19

Figure 3.2 Several Iterations of In-Se Growths on HOPG a.) In_2Se_3 deposition with no island growth, b.) Subsequent deposition to a.) at a lower substrate temperature, c.) In_2Se_3 with no Se background pressure in chamber for $InSe$ growth, d.) $InSe$ growth, e.) Zoomed in image of island shown in d.), f.) $InSe$ growth with higher evaporator voltage. Scanning conditions: a.) 4V, 5pA, b.) 4V, 5pA, c.) 2V, 10pA, d.) 2V, 5pA, e.) 1V, 50pA, f.) 2V, 10pA. . . . 21

Figure 3.3 Height Profiles of In_2Se_3 Islands on HOPG The red lines represent the height profiles taken at each respective island. Scanning conditions: 2V, 5pA. 22

Figure 3.4 AFE and FE Stripe Features on In_2Se_3 Island a.) Large scale image of the surface. The red circle indicates the island shown in the zoomed in images, b.) and c.) are trace and retrace images taken simultaneously, d.) and e.) are trace and retrace images taken simultaneously. Scanning conditions: a.) 2V, 5pA, b.) and c.) 2V, 50pA, d.) and e.) 1.4V, 80pA. 23

Figure 3.5 Sample 13 In_2Se_3 on $NbSe_2$/HOPG A region with multiple layers of In_2Se_3 is shown, where FE stripe features intrinsic to $\beta^* - In_2Se_3$ are visible on both layers. a.) – d.) are STM topography images and e.) – h.) are their corresponding current maps. Scanning conditions: a.) and e.) 2V, 5pA, b.) and f.) 2V, 5pA, c.) and g.) 2V, 50pA, d.) and h.) 2V, 50pA. 24

Figure 3.6 Sample 13 Many FE Domains in In_2Se_3 Corresponding topography images and current maps showing many difference FE domains within different regions of the film. Scanning conditions: a.) and b.) 2V, 10pA, c.) and d.) 2V, 5pA. 25

Figure 3.7 Sample 16 Island Height and Crystallinity in In_2Se_3 on HOPG a.) A short amorphous In_2Se_3 island, with a corresponding height profile shown in b.), c.) Zoomed in image of the island in a.), d.) In_2Se_3 island with a corresponding height profile shown in e.) and an image of the island in f.), g.) FFT image of f.), h.) inverse FFT image of g.). Scanning conditions: a.) 2V, 5pA, c.) 2V, 20pA, d.) 2V, 10pA, f.) 2V, 20pA. 26

Figure 3.8 Sample 14 $NbSe_2$ on HOPG a.) A T-$NbSe_2$ island on bare HOPG, b.) Zoomed in image of the island in a.), showing the CDW, c.) FFT image of b.). Scanning conditions: a.) 2V, 10pA, b.) 2V, 50pA. 27

Figure 3.9 Sample 14 In_2Se_3 on $NbSe_2$/HOPG a.) Several In_2Se_3 islands growing on the edges of $NbSe_2$, with one island growing on top of an $NbSe_2$ island, b.) Zoomed in image of the vertical heterostructure and first layer In_2Se_3 boundary and the corresponding current map in c.), d.) In_2Se_3 lateral heterostructures with $NbSe_2$, e.) Zoomed in image of the boundary between materials and the corresponding current map in f.). Scanning conditions: a.) 2V, 5pA, b.) and c.) 2V, 10pA, d.) 2V, 5pA, e.) and f.) 2V, 5pA. 28

Figure 3.10 Sample 18 In_2Se_3 and $NbSe_2$ Heterostructure on HOPG a.) and b.) show the initial $NbSe_2$ growth, c.) and d.) show the sample after the In_2Se_3 deposition. Scanning conditions: a.) -2V, 20pA, b.) 2V, 10pA, c.) 2.2V, 5pA, d.) 2V, 5pA. 29

Figure 3.11 Height Comparisons of In_2Se_3 and $NbSe_2$ Heterostructure on HOPG In_2Se_3 islands in all images are labeled with text or a red star. All other structures are $NbSe_2$. The white lines indicate a line profile taken at that point, with the measured height adjacent to it. a.) has a region of In_2Se_3 on bare HOPG, while In_2Se_3 in b.) and c.) in on top of $NbSe_2$. The scanning conditions for each image is as follows: a.) -2V, 5pA; b.) 2V, 10pA; c.) 2V, 5pA. 30

Figure 3.12 Crystallinity of Short In_2Se_3 Islands a.) and b.) are In_2Se_3 islands on HOPG. The specific area measured is circled in a.), c.) and d.) are In_2Se_3 islands on $NbSe_2$. Scanning conditions: a.) 2V, 5pA, b.) 2V, 20pA, c.) 2V, 5pA, d.) -1V, 50pA. 31

Figure 3.13 Moiré Pattern STS a.) and d.) are two different In_2Se_3 islands on $NbSe_2$ with the height of the island labeled in each image, b.) Zoomed in image of a.) with key points along a line STS marked with circles corresponding to the colors in c.), e.) Zoomed in image of d.) with line STS moving away from the island edge, shown in f.). Scanning conditions: a.) 2V, 10pA, b.) 1.2V, 50pA, d.) 2V, 20pA, e.) -1.1V, 20pA. STS curves were taken at (c) 1.2V, 50pA and (f) -1.1V, 100pA and the curves are offset to show detail. 32

Figure 3.14 In_2Se_3 STS a.) Boundary between $NbSe_2$ and In_2Se_3 with a black arrow indicating line STS moving away from the boundary, shown in b.). Scanning conditions: a.) 2V, 20pA. STS curves taken at 1V, 20pA and curves are offset to show detail. 33

Figure 3.15 Moiré Pattern STS a.) In_2Se_3 island on $NbSe_2$, b.) Moiré pattern between the two materials, c.) Line STS indicated by the black arrow, with corresponding curves and waterfall plot shown in d.) and e.). Scanning conditions: a.) 2V, 10pA, b.) 0.8V, 50pA, c.) 1.2V, 50pA. STS curves were taken at 1.2V, 50pA and the curves are offset to show detail. 34

Figure 3.16 Examples of Tall In_2Se_3 Structures a.) In_2Se_3 island on $NbSe_2$, wedged between two second layer $NbSe_2$ islands. The red lines represent line profiles with their corresponding height measurements next to them, b.) Core-shell structure, due to In_2Se_3 conforming to the spaces in between $NbSe_2$ islands. Scanning Conditions: a.) 2.5V, 5pA, b.) 2V, 5pA. 34

Figure 3.17 Tall In_2Se_3 and $NbSe_2$ Heterostructure on HOPG Various height profiles measuring the island and surrounding features. Scanning Conditions: 2V, 5pA. 35

Figure 3.18 Tall In_2Se_3 and $NbSe_2$ Heterostructure Features a.) In_2Se_3 island with interesting stripe features, formed on an $NbSe_2$ and laterally next to an $NbSe_2$ island that is either a second layer island on is on a higher HOPG step, b.) and c.) show zoomed in images of the stripe features, d.) The same island after being destroyed by the STM tip. Scanning conditions: a.) and b.) 2V, 20pA, c.) 1.5V, 50pA, d.) 2.5V, 5pA. 36

Figure 3.19 In_2Se_3/$NbSe_2$ Boundaries a.) and b.) are images of the same pair of islands, and c.) and d.) are another pair of islands. Scanning conditions: a.) and b.) 2V, 5pA, c.) 2V, 20pA, d.) 1V, 750pA. 37

Figure 3.20 In_2Se_3/$NbSe_2$ Core-Shell Structure a.) Large scale image showing In_2Se_3 growing in between $NbSe_2$ fully surrounding one island, b.) Zoomed in image of one boundary of the core-shell structure. A triangular domain of $NbSe_2$ is the area shown in d.), c.) Image of the boundary, with some FE features in the In_2Se_3. Scanning conditions: a.) 2V, 5pA, b.) 2V, 10pA, c.) 1.4V, 40pA, d.) -1.2V, 50pA. 38

Figure 3.21 In_2Se_3/$NbSe_2$ Lateral Heterostructure a.) Interface between $NbSe_2$ and In_2Se_3, b.) and c.) are the curves and waterfall plot taken over the black arrow, d.) and e.) are select curves from the same line, between the white lines, to show detail in curves near the boundary. Scanning conditions: a.) 2V, 20pA. STS curves taken at 1V, 20pA and curves are offset to show detail. . . 39

Figure 3.22 Core-Shell STS at Boundary a.) $In_2Se_3/NbSe_2$ boundary, b.) and c.) are the image and line STS on In_2Se_3 along the white arrow, d.) shows a different region of the boundary where line STS was taken on $NbSe_2$ along the white arrow, with corresponding curves and waterfall plot in e.) and f.). Scanning conditions: a.) 2V, 10pA, b.) and d.) 1.4V, 40pA. STS curves were taken at 1.4V, 20pA and are offset to show detail. 40

LIST OF ABBREVIATIONS

CB	Conduction Band
CDW	Charge Density Wave
DOS	Density of States
FE	Ferroelectric
FFT	Fast Fourier Transform
HOPG	Highly Oriented Pyrolytic Graphite
LDOS	Local Density of States
LHe	Liquid Helium
LN2	Liquid Nitrogen
MBE	Molecular Beam Epitaxy
SC	Superconducting/Superconductor
STM	Scanning Tunneling Microscopy
STS	Scanning Tunneling Spectroscopy
TMD	Transition Metal Dichalcogenide
TSP	Titanium Sublimation Pump
VB	Valence Band

CHAPTER 1

INTRODUCTION

1.1 Motivations to Study In_2Se_3/$NbSe_2$ System

1.1.1 Thin Films in Condensed Matter Physics

Condensed Matter physics aims to describe the properties of large collections of atoms that interact due to their proximity, specifically crystalline solids [1]. The growth and characterization of thin film materials provide a platform to study fundamental physics governing these systems of atoms down to the 2D limit, especially in van der Waals materials where minimal inter-layer interactions and high mechanical flexibility are typically observed [2]. 2D systems have a wide array of interesting electronic, magnetic, and correlated physical properties, which have technological applications within optoelectronic devices, field effect transistors, and batteries [3].

1.1.2 Low Dimensional Ferroelectric Materials

Ferroelectric (FE) materials have a spontaneous electric polarization induced by a broken symmetry within the crystal lattice and are used in applications such as the control of superconductors and Mott insulators, as well as components of tunnel junction and spintronic devices [4–7]. Within FE materials, a depolarization field that opposes the polarization, increasing in strength as the thickness of the film decreases [8]. This makes the study of FE materials in ultra-thin film systems difficult, as a material that is FE in the bulk may not be in a thin film [9]. One solution to this problem is to induce a broken symmetry through an inter-layer shift in a bilayer system [10]. There are, however, classes of materials that have robust FE within a monolayer, such as Group IV Chalcogenides [9]. Exfoliation techniques which involve taking layers from bulk material and transferring them to a substrate, yield films down to 1nm in thickness, although the exact thickness is difficult to control [11]. Deposition techniques are also used to prepare these materials, with limitations such as high cost and low crystal quality [11]. The potential for fundamental physics governing these systems and the various applications motivates a broader search for similar materials. More generally, Post Transition Metal Chalcogenide materials have been investigated for their ferroelectric properties, including In_2Se_3 [12, 13].

1.1.3 Potential Heterostructures with $NbSe_2$

Transition Metal Dichalcogenides are often used in ferroelectric heterostructures due to their ability to grow on various substrates, wide range of electronic properties, and higher performance than Si-based semiconductor devices [14, 15]. Heterostructures composed of In_2Se_3 and various TMDs such as MoS_2, $MoSe_2$, and WSe_2 have demonstrated high charge transfer between the materials as well as ferroelectric control of the electronic structure of the TMD component [16–19]. $NbSe_2$ is another TMD with interesting electronic properties, such as metallic and charge transfer insulating phases, CDW phases, and low temperature superconductivity [14, 20, 21]. This makes $NbSe_2$ a good candidate to build upon the previous heterostructure studies.

1.1.4 Designing the Growth

The goal of this study was to achieve a sub-monolayer coverage of both $NbSe_2$ and In_2Se_3 to allow for the formation of both vertical and lateral heterostructures, while growing relatively large scale, atomically flat islands. The growth of both $NbSe_2$ and In_2Se_3 was optimized individually on HOPG, before growing heterostructure samples. A difference in the growth dynamics of In_2Se_3 was observed between these cases. While previous studies have been conducted, from large-scale coverage of In_2Se_3 films, to sub-monolayer coverage in heterostructure studies and growth dynamics studies, the goal of this thesis is to explore the growth dynamics of In_2Se_3. In the pursuit of atomically smooth islands, interesting observations were made about the growth and interactions with $NbSe_2$ [17, 18, 22–25].

1.2 Epitaxial Thin Films

1.2.1 Growth Dynamics

During epitaxial growth, the substrate imposes its own crystallinity and symmetry onto the grown film. The growth dynamics of thin films can be described by several parameters. Adsorbates, atoms or molecules that are deposited onto a surface, may have enough energy to re−evaporate off the surface in a process called desorption. Those that remain may diffuse across the surface if the energy of the adatom is higher than the diffusion barrier. Eventually, adsorbates with will settle, or nucleate, at a specific site. Terraces are single layer areas of the film, the edges of which require

energy for the adsorbates to descend. If an adsorbate doesn't have enough energy to descend the step edge, it remains on that layer [26].

When the system is at thermodynamic equilibrium, i.e. the rate of adsorption is equal to the rate of desorption, it is described by one of three thermodynamic growth modes [27]. These growth modes depend upon the differences in surface tension between the top layer of material and the vacuum, the substrate and the vacuum, and the top layer and substrate. The relationship between these surface tensions determines if the growth mode will be 2D or 3D [26]. The Frank-van der Merwe (FM) growth mode, also called layer-by-layer or step-flow growth, is characterized by adatoms that nucleate on the edges of established islands, yielding an overall 2D morphology. The Volmer-Weber (VW) growth mode, 3D island growth, occurs when laterally small and tall islands are formed due to adatoms nucleating on the tops of established islands. The Stranski-Krastanov (SK) growth mode is a combination of the two, where the growth is 2D until a critical thickness, and is also called layer-plus-island growth. When the system is far from equilibrium, it is described by kinetic growth modes. Step-flow growth occurs when a single layer grows at a time and the adsorbates have enough energy to descend the step edges of the existing layer. Layer-by-layer growth occurs when two layers are growing at a time, since some adsorbates can descend the step edges, while there is another layer forming on top of this first layer. Multilayer growth yields films much rougher than the other two growth modes, as multiple layers are growing simultaneously [26].

Understanding these growth modes is important when designing a thin film growth, in order to produce an ideal sample for the intended scientific study and application. A smooth, uniform film is the ultimate goal, as defects and grain boundaries within the film can affect the properties of the material and make the study of the material properties more complicated [28]. Carefully choosing the growth parameters allows us to strike a balance between diffusion and nucleation on the substrate surface and achieve a uniform film growth. The substrate temperature during growth is an important parameter, as it affects both the diffusion and nucleation of adsorbates on the surface, in turn affecting the quality of the film [anisotropic]. The interaction between the adsorbates and

the substrate will also influence the growth of the film, determining the orientation of the film and the precise energy requirements for the film to grow in a particular growth mode [27, 29]. The substrate can influence many properties of the thin film by inducing mechanical strain, donating or depleting charge through charge transfer, among other mechanisms [30].

Typical thin film growths yield thermodynamically stable phases of materials, but under certain circumstances metastable structures and phases of materials are stabilized. This typically consists of a structural change within the crystal structure of a material, such as an amorphous-crystalline transition in phase change alloys, or a slight change in buckling in TMDs [31]. External stimuli like laser pulses or mechanical strain may be used to cause this transition in these material systems [31–33]. A carefully designed growth can automatically yield a metastable structure or phase of a material, due to mechanical strain induced by a substrate or secondary material, a specialized growth mechanism to crystallize an amorphous film, or chemical doping [32, 34]. Intercalation of atoms between the layers of a film can also stabilize structures that are otherwise thermodynamically unstable [35].

1.2.2 Overview of Heterostructure Studies

Epitaxial growth implies some interaction between the material film and substrate, and therefore an influence on the structural and physical properties of the film [26, 30]. It is also useful to combine materials into heterostructures to study the effects of each material on the other, whether the materials are stacked vertically or laterally adjacent to one another. One of many considerations when designing a heterostructure is the lattice mismatch, or relative mismatch between the lattice constant of each material [27]. When considering the energy cost versus energy gain in strained systems, it may be more energetically favorable to distort the lattice under this strain, causing distorted regions of the crystal close to the interface of the two materials [27]. The symmetry of each component of the heterostructure is an important consideration, since a film will often grow with specific orientations along high symmetry directions of the layer beneath it [36]. A difference in the work function of each material, the minimum amount of energy required to remove an electron from a material, will induce charge transfer between materials as electrons flow to the

material with the higher work function to bring the Fermi levels of each material to equilibrium [27]. In semiconductors, an effect called band bending will occur, as band edges of both materials with bend towards each other in order to equalize their respective Fermi levels [27].

Heterostructure studies often focus on the proximity effects between interesting electronic or magnetic phases of materials. Ferroelectric materials are used in heterostructures to influence the properties of another material, typically a Mott insulator or superconductor [5, 6, 37]. In device applications, the FE polarization is used as a switch to switch between specific states, typically in the context of a transistor [37]. Heterostructures can also induce novel and exotic phases within materials. Topological superconductors and unconventional FE in Moiré systems are both phases whose physical properties are studied using heterostructure systems [38, 39].

1.2.3 Van der Waals Materials

Van der Waals materials have weak vdW inter-layer interactions as opposed to strong covalent bonds [40]. Since vdW materials are layered, exfoliation techniques can be used to cleave layers from the bulk crystal to produce a thin film sample [11]. However, the lack of dangling bonds between layers allows for the direct growth of heterostructures with relatively large lattice mismatch, making vdW materials ideal for thin film study [40]. Despite the weak interactions between layers, lattice mismatch and symmetry are important to consider when designing heterostructures. Strain relaxation in vdW materials occurs immediately in the first layers grown on a substrate, unlike strain relaxation in 3D materials that depends on the film thickness and occurs gradually over several material layers as the film gets thicker [41]. This strain relaxation is typically characterized by shifts in the weakly interacting layers as opposed to dislocations, and the strain is determined by the initial lattice mismatch between it and the substrate [41]. The effect of strain in vdW materials has been shown to affect the electronic properties of the films, such as changes in the CDW order bandgap [42–44].

The interactions between a film and different potential substrates are important to consider when designing a growth. The following example shows MBE depositions of WSe_2 on two different substrate materials. There is a significant difference between the growth rate of the film

on graphene/SiC in comparison to the HOPG, as shown in Fig.1.1. There are several material layers of WSe_2 present on each surface, such that the respective substrates are mostly covered in both images. In half the deposition time, a similar coverage was achieved on graphene/SiC Fig.1.1b versus HOPG Fig.1.1a. Understanding these differences is imperative to achieving the target coverage of material during thin film growth.

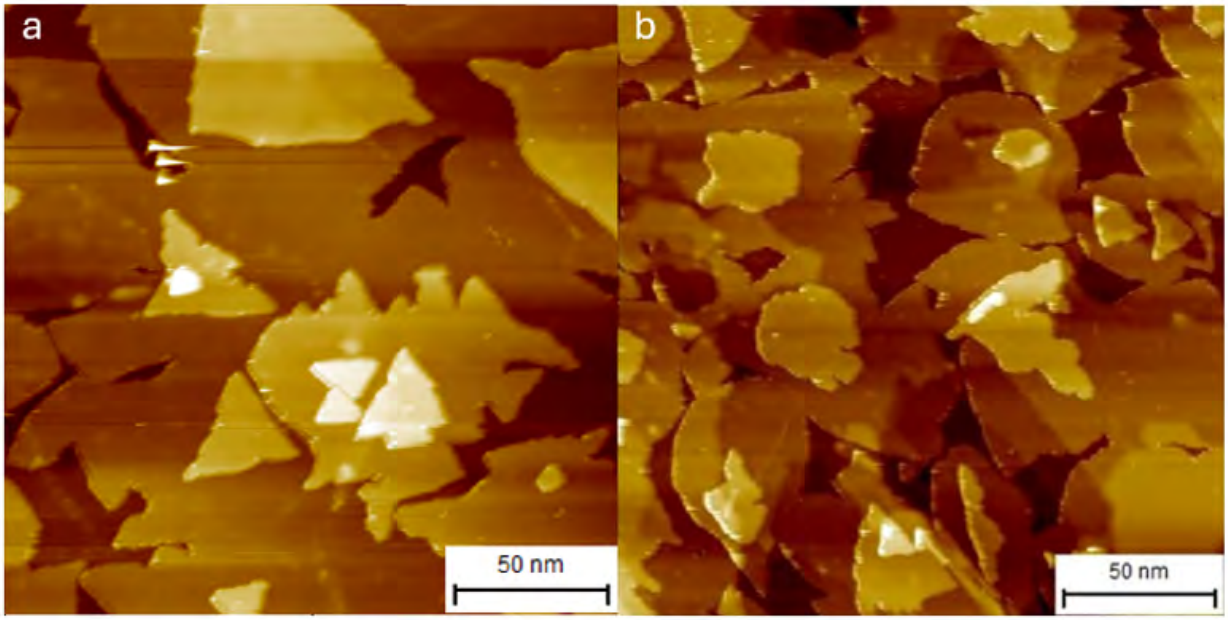

Figure 1.1 WSe_2 Growth on Different Substrates a.) HOPG substrate, b.) graphene/SiC substrate

1.2.4 Transition Metal Dichalcogenides

Transition Metal Dichalcogenides are a popular class of materials that have the chemical composition MX_2, where M is a transition metal and X is a chalcogen (S, Se, Te). They are vdW materials and therefore have strong covalent intra-layer bonds with weak inter-layer interactions [40]. These materials have been extensively studied, exhibiting a wide array of properties and phases that make them versatile components in thin film heterostructure studies [45]. Since TMDs are well studied, there are many studies that describe their growth. Since our group has experience growing various TMDs, we also have an understanding of how to grow them with MBE, as is discussed in Section 2.1 [46, 47].

1.3 Moiré Pattern Background

1.3.1 Overview

A Moiré pattern is a long-range periodic pattern formed between several material layers in a vertical heterostructure that has a lattice mismatch and/or a non-zero twist angle between them [48]. The Moiré potential describes the potential energy associated with the pattern and depends on the inter-layer coupling and mechanical strain between the layers of the material [48]. Variations in the Moiré pattern affect the Moiré potential and therefore affect the electronic properties of the system, which can be characterized through local probes such as STM [49]. Moiré patterns are studied in bilayer systems of the same material and heterostructures of different materials, depending on the physical properties and applications of interest [50].

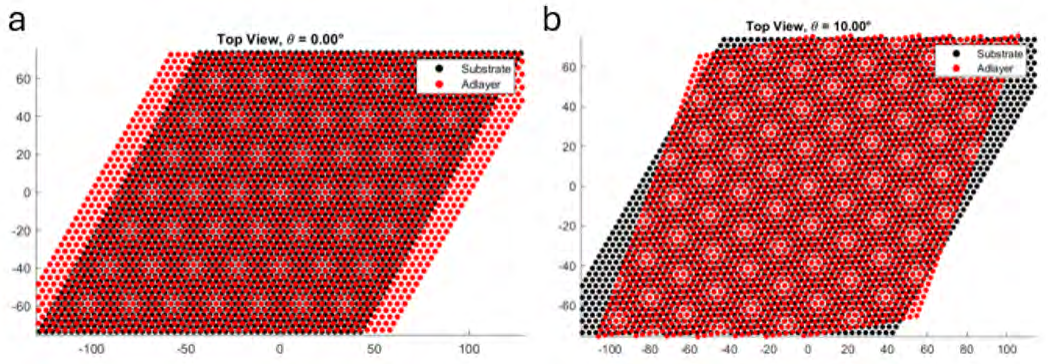

Figure 1.2 Simulated Moiré patterns for hexagonal lattices with either a lattice mismatch or a rotation angle between layers, a.) The substrate and adlayer lattice constants are 3.4Å and 4.0Å, respectively, b.) Both layers have a 3.4Å lattice constant, which a twist angle of 10^o. The code used to create these images was created and refurbished by other graduate students in the group.

1.3.2 Interesting Physics Examples

Moiré patterns often correspond to local variations in the electronic properties of the system, often characterized by the change in the band structure such as induced states within the bandgap of the system [51, 52]. The electronic variation and corresponding strain can be mapped to understand the effects on the system as a whole [53]. The effects of Moiré patterns are also studied, such as unconventional FE induced in heterostructures, which induced a FE polarization through broken symmetry over several material layers as opposed to FE monolayers that have a broken symmetry

already within their crystal structure [39]. FE materials are also used to control the Moiré potential, and flat band physics observed within the Moiré patterns of FE materials [54, 55]. More generally, Moiré patterns are studied for their associated correlated insulating phases, non-trivial topology, and unconventional superconducting phases [50].

1.4 Lateral Heterostructure Background

1.4.1 Lateral versus Vertical Heterostructures

Vertical heterostructures are useful when studying Moiré patterns and any induced effects on the surface layer, but the full details of the interaction between the constituent materials may remain unclear. Lateral heterostructures allow the direct study of the interface between two materials. When using local probes like STM, effects like band bending and interface states are directly observable [56]. It is also possible to measure how far from the interface the observed phenomena are observed [57]. Studies of a lateral heterostructure interface are often used to deepen the understanding of previous works [17, 18]. Despite challenges related to the stability and quality of the atomic structure at the interface, lateral heterostructures provide a unique platform to explore the properties of thin films [58].

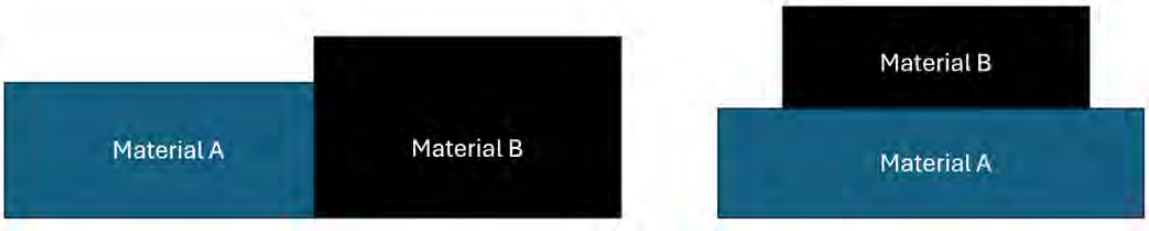

Figure 1.3 Lateral Heterostructure (left) versus Vertical Heterostructure (right)

1.5 In This Thesis

This thesis will discuss the interesting observations of the growth of In_2Se_3 on bare HOPG and as a heterostructure with $NbSe_2$. This thesis is organized as follows. The Experimental Methods used for this study are discussed in Chapter 2. Chapter 3 contains a review of the material properties, as well as the observations of the growth and an analysis of the various properties observed. A summary of this discussion is presented in Chapter 4.

CHAPTER 2

EXPERIMENTAL METHODS

2.1 Molecular Beam Epitaxy

2.1.1 Overview

Molecular beam epitaxy (MBE) is the growth technique used to create samples, which involves heating ultrapure source materials and depositing them onto a substrate and allowing them to organize themselves into thin films [26]. MBE differs from other deposition techniques, using lower growth temperatures and shorter growth rates, making it ideal for smaller scale studies of materials [27]. These slower growths can produce atomically smooth films, with more control of the growth overall in terms of the layer thickness, film composition, and doping [59]. As a result, MBE grown films are sensitive to the environment in which they are grown, and depositions must be conducted at ultrahigh vacuum to avoid contamination from the chamber [26, 59]. The dynamics of thin film growth as discussed in Chapter 3 are fundamental to the MBE deposition process. The growth parameters determine these dynamics, therefore affecting the quality of the film [26]. The substrate temperature, flux of source material deposited to the surface, and even the relative positions between the evaporators and substrate can affect whether the film is uniform in thickness and composition [59]. Annealing, heating the sample after the deposition of material, can help to improve the overall crystallinity of the film and allow for additional island formation [26].

2.1.2 Our System

Our lab uses an Omicron MBE system. The chamber is maintained by mechanical, turbo, and ion pumps during normal operation, which keeps the chamber at a base pressure between high $E-10$ and low $E-9$mbar. The ion pump is turned off during material depositions. A titanium sublimation pump (TSP) is occasionally used to improve the pressure. Because the system operates in ultrahigh vacuum, extra care needs to be taken to prevent raising the chamber pressure, including only using vacuum safe materials and monitoring the pressure for any potential leaks. The chamber is cooled with LN2 when working in the chamber, to maintain the pressure and avoid contamination

of the thin films during deposition.

The sample stage holds the sample plate upside down, so that the substrate is pointing towards the material sources at the bottom of the chamber. The stage is capable of heating the sample, either by direct current heating which sends a current through the substrate to heat it, or by resistive heating which sends a current through filaments near the sample plate to produce heat. Direct current heating is useful for applications like graphitizing SiC, discussed in section 3.2.1, but in all other applications resistive heating is used. A thermocouple near the sample plate and heating filaments reads an approximate substrate temperature. There are several material sources at the bottom of the chamber, which are used to deposit materials onto the substrate. Two e-beam evaporators, one for Nb and one for bulk In_2Se_3, were used. A thermal cracker cell was used to deposit Se.

When working with any equipment or materials that have been exposed to ambient pressure, in situ cleaning is required. New material sources undergo a degassing process, which is the process of slowly heating a UHV component to evaporate contaminants of said component and allowing the vacuum pumps to remove the contaminants from the chamber. The degassing temperature must be higher than the deposition temperature that will be used during the deposition, to remove all contaminants that could potentially be released at the deposition temperature. New substrates are loading into the system through a load lock, or smaller chamber that can be pumped down to vacuum and vented to ambient pressure relatively quickly. After a substrate is moved into the MBE chamber, it needs to undergo a similar degassing process to clean any potential contamination on the substrate and sample plate, which would increase the chamber pressure and disrupt the film growth.

2.2 Scanning Tunneling Microscopy

2.2.1 Overview

The theory behind the Scanning Tunneling Microscope has been extensively studied since its invention, which would earn half of the Nobel Prize in 1986 for its contributions to the field [60, 61]. A bias voltage is applied between the microscope tip and sample, which are brought within

close proximity, typically between 3 and 10Å [62]. An STM tip must metallic and near atomically sharp to achieve a sharp image, since the apex of the tip is what establishes the tunneling current with the sample [63]. The electron orbitals of the tip and sample interact, known as orbital overlap, making the tip sensitive to the individual atoms within a crystal and producing an image with atomic resolution [62].

Quantum tunneling is the dominant mechanism behind STM. When the tip and sample are within STM range, there is a high tunneling probability [62]. The tunneling current can be expressed as an integral over the energy states of the system,

$$I \propto \int_0^{eV} \rho_S(E_F - eV + \epsilon)\rho_T(E_F + \epsilon)|M|^2 d\epsilon, \tag{2.1}$$

where E_F is the Fermi energy, and ρ_S and ρ_T are the density of states of the sample and STM tip. The tunneling matrix, $|M|$, is determined by the wavefunctions of the tip and sample near the center of the vacuum gap between them, but is usually taken to be constant in the tunneling current equation [62]. The tip is sensitive to the surface states of the sample and measures the convolution of the surface topography as well as the local density of states (LDOS) at a given area of the sample [27]. Consequently, the apparent height of features in an image is not necessarily the physical height, since there may also be a difference in the LDOS that is affecting the measured tunneling current.

Scanning tunneling spectroscopy is a technique to study the electronic properties of a material at a specific point on at surface. The differential conductance, defined as,

$$dI/dV \propto \rho_S(E_F - eV). \tag{2.2}$$

is directly proportional to the LDOS, and can be directly measured using STS [62]. An important assumption for STS is that the density of states of the tip is negligible, which is an important consideration when conducting experiments [27].

2.2.2 Our System

Our lab uses an Omicron low temperature (LT) STM. We typically operate at 77K, filling the chamber with LN2 every 48 hours to maintain this temperature. The STM has the capability to operate at LHe temperature, but this study was only conducted at LN2 temperature. The base pressure is 1-2 $E-11$mbar, which is maintained by an ion pump. Samples are kept in a carousel in the STM chamber and are transferred into the STM stage when studied. The STM is sensitive to vibrations, so the chamber is suspended by various springs to minimize the noise in the environment. Before imaging the real samples, the STM tip is conditioned by scanning a metallic surface, either Ag or Cu, to verify the sharpness and resolution. Test STS curves are also taken and compared to the well-known curves for these materials, to ensure that the tip is not imposing any features in the STS curve so that the assumption of a negligible tip density of states holds. STS measurements are taken using a Lock-In amplifier, which compares an input signal to a reference signal to isolate that specific frequency using Fourier transforms. Experimentally, the dV in equation 2.2 is an AC modulation sent to the tip and the response to that signal is the dI in the equation. This Lock-In technique allows for the direct measurement of the differential conductance, which is directly proportional to the density of states of the material being measured. It is often useful to take STS curves along a line to see the variation in electronic properties over a specific region.

CHAPTER 3

MATERIAL GROWTH AND THE STRUCTURES ON THE SAMPLES

3.1 Material Properties

3.1.1 Niobium Diselenide, $NbSe_2$

Niobium Diselenide, $NbSe_2$, is a TMD with a lattice constant of ~3.4Å and hexagonal symmetry [64]. At the monolayer regime, it can exist in two different stacking configurations, 2H and 1T, each with different physical properties [21]. H-$NbSe_2$, stable in the bulk and in the 2D limit, is metallic and has a SC transition temperature of ~7K and CDW transition temperature of ~34K in the bulk [64–66]. T-$NbSe_2$ is not stable in the bulk and has a $\sqrt{13} \times \sqrt{13}$ CDW phase with a transition temperature above room temperature [21]. The $\sqrt{13} \times \sqrt{13}$ CDW induces mott physics in T-$NbSe_2$, which is considered a charge transfer insulator since the Lower Hubbard Band is below the valance band [20, 21]. T-$NbSe_2$ has similar properties to other TMDs like 1T-$TaSe_2$ down to the monolayer regime, allowing for the study of these mechanisms in the 2D limit [67–69]. The proximity effects in heterobilayers of H and T phase $NbSe_2$ have exhibited inter-layer interactions that affect the electronic properties of the materials, such as inducing the Kondo effect [70, 71].

Understanding the growth and formation of each phase of $NbSe_2$ was an important first step to be able to study this interesting TMD. Early studies of T-$NbSe_2$ involve tip-induced phase transformation, typically using voltage pulses from a microscope tip to convert H-$NbSe_2$ into the T phase, sometimes in a reversible process [64, 69]. T-$NbSe_2$ can also be grown directly, forming at a higher substrate temperature than H-$NbSe_2$ [72]. Mixed phase samples are also achievable at intermediate temperatures, and substrates like HOPG and graphene are common substrate choices [21, 73]. The $Se : Nb$ flux ratio present during the deposition can affect the properties of the islands formed, allowing for the formation of a stripe CDW phase at lower ratios [74].

$NbSe_2$ has been studied for its various interesting properties and potential applications. H-$NbSe_2$ exhibits superconductivity that is robust to relatively high magnetic fields, making it a platform to study various properties of superconductivity, especially in proximity to other interesting materials such as topological insulators [65, 75]. The superconducting phase of H-$NbSe_2$ can be

influenced and tuned when included in certain heterostructures, intercalated with material, and when adsorbates are deposited onto the surface [73, 76]. For the intercalation case, the enhancement of the superconducting properties is accompanied by stabilizing a novel compound within the vdW layers of $NbSe_2$ [35, 77]. As previously stated, both H and T phases have CDW states. The Star-of-David CDW in T-$NbSe_2$ is correlated with the Mott physics observed in the material, the packing of which is dependent on the size of the island [72, 78, 79]. Understanding the electronic features of the Lower and Upper Hubbard Bands, such as their location below the valence band and relationship with the CDW respectively, is important to explore possible applications, such as in doped Mott insulator systems [20, 80]. In H-$NbSe_2$, the CDW is sensitive to defects such as atomic vacancies and intercalants, which can locally affect the amplitude of the CDW and allow the CDW to survive above the transition temperature [81, 82]. Strain can also affect the properties of the CDW, whether they are local defect related strain fields or a larger scale strain that changes the order of the CDW entirely [42, 82].

3.1.2 In-Se based Materials

Indium Selenides, In-Se based materials, are layered Post Transition Metal Chalcogenide materials that have been studied for large scale device applications [83]. These materials are highly polymorphic, meaning there are several thermodynamically stable stacking configurations at specific stoichiometries, with $InSe$ and In_2Se_3 being the most common In-Se compositions [13]. The amount of available Se during the growth and anneal processes can determine the population of $InSe$ and/or In_2Se_3 formed on the sample [84]. Several polymorphs of both $InSe$ and In_2Se_3 have lattice constants of ~4Å, with various electronic properties [83, 85]. A summary of reported bandgaps is shown in the table below. Note that there are discrepancies in the reported monolayer bandgap for $InSe$, with some reports of the unstrained bandgap being closer to $1.4eV$, similar to $\alpha - In_2Se_3$ [84]. Others claim that this $1.4eV$ gap is for few layer $InSe$ [86]. Other stoichiometries of In-Se based materials have been reported, including In_3Se_4, In_4Se_3, and a metastable compound $InSe_2$ stabilized between the vdW gaps in $NbSe_2$ [35, 87]. These materials have potential applications for thermoelectric and switchable ferroelectric devices, making them interesting for

extensive local probe studies using techniques such as STM [85, 88].

In-Se Electronic Bandgaps		
Material	Bandgap $[eV]$ (ML)	Reference
$\beta - InSe$	2.3*	[89]
$\gamma - InSe$	2.3*	[87, 89]
-	-	-
$\alpha - In_2Se_3$	1.4	[13]
$\beta' - In_2Se_3$	2.5	[13, 90]
$\beta^* - In_2Se_3$	2.5	[13, 90]

$InSe$ is composed of four atomic layers, where the two central layers are In and the outer layers are Se [10]. An indirect to direct bandgap transition, as well as an insulator to metal transition, have been theoretically predicted in $InSe$, motivating the study of the material [87]. There are several polymorphs, the most notable of which are the γ and β phases, which have different stacking configurations within their layers [91]. $\beta - InSe$ exhibits both in-plane and out-of-plane FE down to the monolayer regime [10]. The superconducting and CDW properties of $InSe$ can be tuned through doping, as high hole doping forces the system into the CDW phase, preventing SC entirely [92]. The CDW in hole doped $InSe$ coexists with ferromagnetic ordering, motivating the study of the material's magnetic properties [93].

While $InSe$ has many interesting properties, our main interests focused on In_2Se_3 heterostructures, which is composed of five alternating atomic layers of Se and In, where the outer and central layers are Se [10, 87]. The α polymorph has both in-plane and out-of-plane FE, while the β polymorph has in-plane AFE in its β' variant and in-plane FE in its β^* variant [13]. $\beta - In_2Se_3$ is stable at room temperature and condenses into β' at $\sim$180K and condenses further into β^* below this [13]. Note that throughout the literature, β^* is also referred to as β'' or $\alpha\prime$ in some cases, but for the purpose of this thesis, the In_2Se_3 phase with a zigzag FE stripe feature will only be referred to as β^* [13, 94]. In_2Se_3 has been studied for potential device applications, therefore many previous studies have discussed the growth of large scale films, on the micron scale [22, 24, 25]. There

are studies, however, on the stages of island growth before the formation of the full 5-layer In_2Se_3 structure, demonstrating that partial layer growth is possible in some circumstances [23].

α, β', and β^* phase In_2Se_3 each have various FE properties that make them exciting materials for thin film studies [13]. $\alpha - In_2Se_3$ has two possible stacking configurations, 2H and 3R, differentiated by the intra-layer stacking of the covalently bonded 5-layer structure and the inter-layer stacking between layers [91, 95]. It has robust FE down to the monolayer at room temperature, and when heated to ~473K it undergoes a transition into the paraelectric β phase [96, 97]. The in-plane and out-of-plane ferroelectric polarizations are strongly correlated and the polarization directions of each layer in multilayer $\alpha - In_2Se_3$ will affect the overall polarization [98, 99]. $\beta - In_2Se_3$ has purely octahedral symmetry within its crystal structure, which is slightly less energetically favorable than $\alpha - In_2Se_3$ since it has a combination of octahedral and tetrahedral symmetry, although both phases are stable at room temperature [13, 91]. $\beta - In_2Se_3$ condenses into the AFE β', which is characterized by an alternating stripe feature, and FE β^* phase which is characterized by a zigzag stripe feature [100]. These phases can coexist on a surface and the structural transition is reversible [90, 94].

In_2Se_3 has many potential applications due to its various FE phases, making it an interesting candidate for heterostructure studies. The band structure and bandgap of In_2Se_3 is sensitive to strain around defects or within a heterostructure, in some cases causing large increases in the bandgap [101]. The contact properties of In_2Se_3 and metallic TMDs, including $NbSe_2$, are affected by the number of In_2Se_3 layers which allows for the construction of more efficient semiconductor devices [102]. The study of these systems as vertical heterostructure helps to understand the overall electronic effects of the heterostructure, while lateral heterostructures make the direct study of potential interface states possible, providing even more context to the structure as a whole [17, 18]. The band character at the interface of these heterostructures can be externally controlled with a FE material, where an electric field is used to switch the polarization direction, essentially acting as an on/off switch to affect the electronic properties at that interface [103]. Beyond switching the polarization direction, the electric field induced by an STM tip can manipulate the FE domain

boundaries of the In_2Se_3 [104]. This FE controller technique can also be used in heterostructures with topological insulators, using In_2Se_3 to control the topological states of the other material [105]. In_2Se_3 was predicted to have nontrivial topology depending on the stacking of multilayer systems and their respective FE polarization directions, making the precise atomic structure and stacking of particular interest in this material system [106]. In fact, the ferroelectric phases of α, β', and β^* are all attributed to the specific location of the central Se atom within the 5-layer crystal structure [101, 107].

3.2 Growth Parameters

3.2.1 Substrate Choice

The choice of substrate was carefully considered when designing the growth. Highly oriented pyrolytic graphite (HOPG) is a commonly used layered material and was the chosen substrate for most of the sample growths discussed in this thesis. HOPG substrates used for sample growths were ultrasonicated with acetone and isopropyl alcohol, then cleaved to reveal a clean and flat surface. The substrates are then degassed in situ at high temperature to further clean the substrate before growth. Graphene is a popular 2D material that has been extensively studied since its discovery and was also considered as a potential substrate. A common technique to produce a graphene substrate for thin film growth is to convert a SiC substrate into graphene [108]. SiC wafers were sliced into individual substrates with a high precision saw and chemically cleaned based on RCA and Piranha cleaning procedures [109, 110]. After chemical cleaning, the substrates were ultrasonicated and degassed in the same process as the HOPG substrates. The surface of the SiC samples were converted into graphene through a process called graphitization, in which the SiC is rapidly heated and cooled to sublime the Si and allow the leftover C to reorganize into graphene [108]. The morphology of the graphene is dependent on the graphitization process as well as whether the surface is Si-terminated or C-terminated [108, 111]. We graphitized Si-terminated SiC substrates, which typically yields a smoother morphology with a more ideal surface reconstruction [111]. Due to the uncertainties of the graphitization process, however, the overall surface morphology was not as flat as HOPG, and therefore subsequent samples were grown on HOPG substrates. An example

of a graphene/SiC sample is shown in Fig.3.1.

3.2.2 $NbSe_2$ Deposition

Pure Nb source material was evaporated simultaneously with pure Se source material, allowing the $NbSe_2$ to form on the substrate. During the deposition, there was a supersaturation of Se in the chamber, raising the chamber pressure from ~1-2e-9mbar to 1-2e-8mbar. This background Se pressure will be referred to as the normal Se pressure, since it is the typical background pressure of Se used when growing TMDs in our system. The deposition of Nb does not significantly affect the chamber pressure. The flux current and deposition time are key factors when tuning the coverage of $NbSe_2$ on the substrate. In general, a ~50nA flux current was used to fix the nucleation rate of material, so the deposition time could act as a gauge to control coverage. An exception to this is when the goal for a particular sample was to grow lateral heterostructures, in which case a ~20nA flux was used to ensure there was plenty of bare substrate on the surface. Since T-$NbSe_2$ typically forms at a higher temperature than the H-phase, the substrate temperature was used to control the population of each phase on the sample. For our samples we used a range of substrate temperatures that allowed for the formation of both H and T phase $NbSe_2$. After the $NbSe_2$ growths, there is typically a population of atoms or clusters that did not aggregate into an island and remain on the substrate surface, which are visible in Fig.3.1. The graphene/SiC sample has a much higher coverage than the HOPG sample, indicating a higher sticking coefficient. However, since the graphene layer is not uniform in thickness, and the $NbSe_2$ islands conformed to this morphology, studying the electronic properties of the material would be more complicated, especially if a second material was deposited.

3.2.3 In_2Se_3 Bulk Material Deposition

For the In-Se structures, bulk In_2Se_3 was evaporated and deposited onto the substrate. The goal was to emulate the growth conditions in Reference [22], such that the amount of Se present in the chamber could be used to selectively grow $InSe$ or In_2Se_3. The evaporator voltage was especially important in this case, to ensure enough energy was provided to fully break down the material. The growth dynamics of In-Se have been modeled in Reference [112], discussing the different diffusion

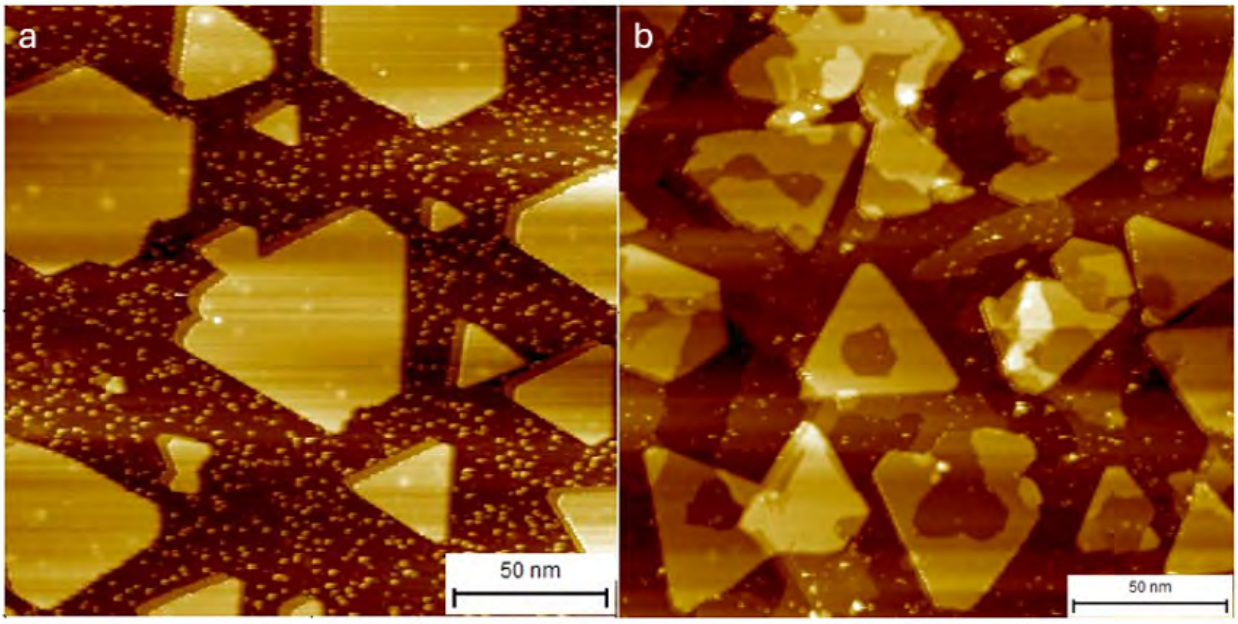

Figure 3.1 $NbSe_2$ Growth on Different Substrates a.) HOPG substrate, b.) graphene/SiC substrate. Scanning conditions: a.) -2V, 10pA, b.) 2V, 10pA.

paths of In and Se on the surface. In the following section, the optimization of the growth including considerations the roughness of In_2Se_3 islands, overall surface morphology, and ratio between In and Se during the deposition, are discussed.

3.2.4 Improving Sample Quality

An extensive literature review was conducted to find approximate growth parameters for an initial test growth after which test growths were performed [13, 21, 23, 64, 74]. STM imaging was used to determine the quality of the film by studying the overall morphology of the sample, checking apparent heights of islands to compare to the expected height of the target structure, and achieve atomic resolution to see the crystal structure. STS curves are also useful to measure the electronic density of states of the structure. When designing a heterostructure sample, the growth temperature of each material determines the growth order, as the material with a higher substrate temperature needs to be grown first or there is the risk that the other material will decompose. $NbSe_2$ was therefore deposited first on heterostructure samples and imaged to verify the quality and coverage of the film. Due to the nature of MBE depositions, assistance was required to conduct some experiments. For longer depositions, another graduate student in the group assisted with

managing the evaporator and substrate temperatures, as well as the flow of LN2 into the chamber for cooling. This student also took supplemental STM/STS on several samples. Although that data is not represented in the figures, it was helpful to paint a fuller picture of the material system, hence this acknowledgment of that contribution.

Many iterations of test In-Se depositions were performed in order to improve island growth on HOPG. In some cases, a subsequent growth on the same HOPG surface would take place, in an attempt to improve the surface quality of that sample. Most often, however, a clean HOPG surface was used for each growth to fully understand the consequences of changing certain growth parameters. The substrate temperature, evaporator temperature, deposition rate, and Se background pressure in the chamber were tuned based on previous growths, to find the most ideal combination of parameters for this material system. Fig.3.2 shows several key stages of the growth optimization. Initial In_2Se_3 growth attempts Fig.3.2a, conducted under the normal Se background pressure, left a high coverage of clusters on the surface that didn't aggregate into islands. We attempted another growth with a higher flux current to increase the growth rate, but islands still did not form. This can indicate that the substrate temperature is incorrect, either too high causing any islands formed to decompose, or too low such that the adatoms don't have enough thermal energy to diffuse on the surface. Since our initial substrate temperature was relatively high, we chose to lower the substrate temperature for future growths. At this higher flux current and lower substrate temperature, islands were able to form. The growth rate of islands was still low, so several consecutive growths on the same HOPG substrate with a high flux current were performed, in case the surface morphology would improve after the formation of a wetting layer and additional material layer, similar to [46]. However, the morphology of the surface didn't significantly improve, shown in Fig.3.2b. One final deposition was conducted with the normal Se background pressure, and a lower flux current still did not decrease the overall roughness of islands or increase the average island size. Since the ratio of Se during the growth was an important factor, and much lower Se ratios were used in ref.[22], we hypothesized that the supersaturation of Se in the chamber was disrupting the diffusion of other material on the surface.

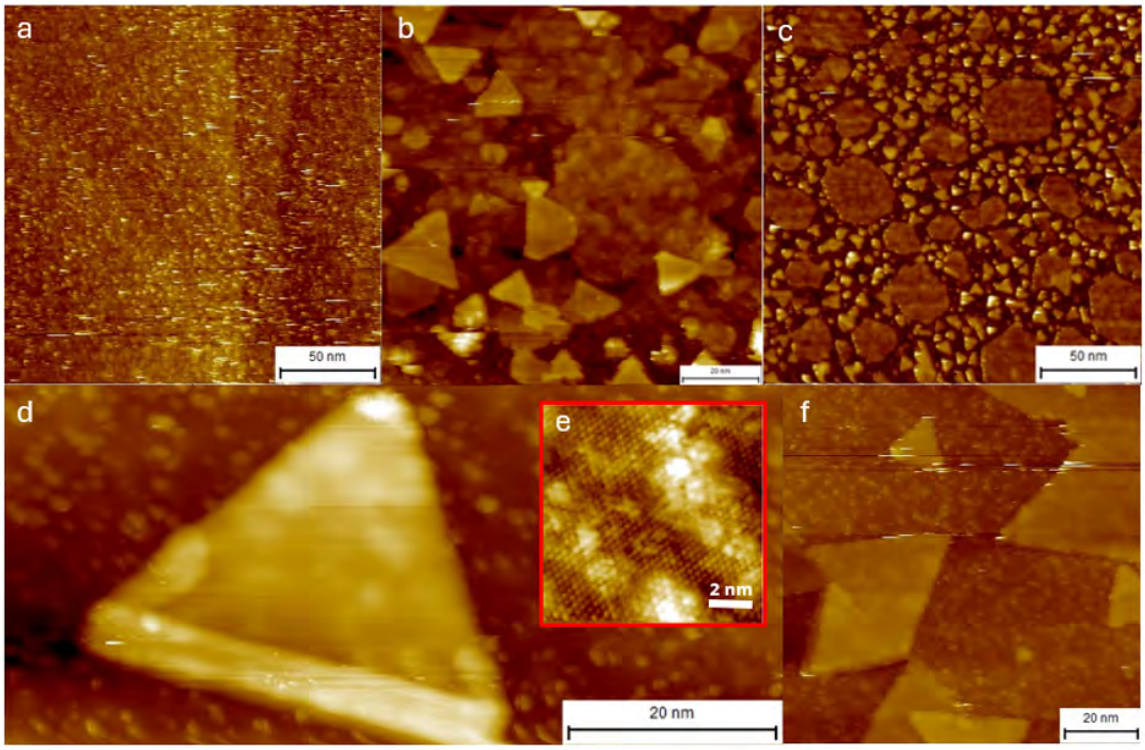

Figure 3.2 Several Iterations of In-Se Growths on HOPG a.) In_2Se_3 deposition with no island growth, b.) Subsequent deposition to a.) at a lower substrate temperature, c.) In_2Se_3 with no Se background pressure in chamber for $InSe$ growth, d.) $InSe$ growth, e.) Zoomed in image of island shown in d.), f.) $InSe$ growth with higher evaporator voltage. Scanning conditions: a.) 4V, 5pA, b.) 4V, 5pA, c.) 2V, 10pA, d.) 2V, 5pA, e.) 1V, 50pA, f.) 2V, 10pA.

Because the high Se background pressure was complicating our understanding of the growth, we conducted several depositions with no additional Se pressure. During these depositions, only the bulk In_2Se_3 source was used, theoretically putting our growths in the $InSe$ growth regime [22]. Fig.3.2c shows a sample after one deposition with a high Se background pressure and one deposition with no Se background pressure. There was a high population of small smooth islands in between rougher, irregularly-shaped islands, which was a promising sign for the next deposition on a clean HOPG substrate. Another parameter we tuned was the evaporator voltage, which is related to the amount of energy used to break down the source material so that it can be deposited onto the surface. Since we were working with a bulk material source, the evaporator voltage needed to be sufficiently high to break the material down into atoms as opposed to large clusters that may affect how the material diffuses and nucleates on the surface. Incrementally raising the

evaporator voltage, Fig.3.2d,f, seemed to produce smoother islands with a more regular triangle shape. Through combination of raising the evaporator voltage to further break down the source material, lowering the flux current to slow down the growth to improve island roughness, and extending the growth time to compensate for the slower growth, a final growth condition was found for growths with no Se background pressure.

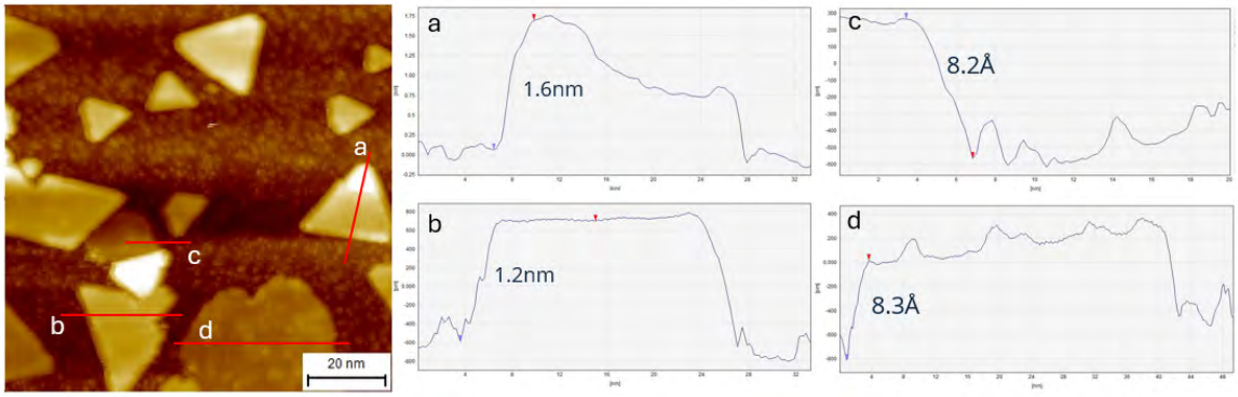

Figure 3.3 Height Profiles of In_2Se_3 Islands on HOPG The red lines represent the height profiles taken at each respective island. Scanning conditions: 2V, 5pA.

After $InSe$ islands were successfully formed with no additional Se, further growths were conducted with similar parameters and a much lower Se background pressure than the normal Se background pressure. The chamber pressure went from ~1-2e-9 mbar to ~5e-9 mbar during the deposition, and the addition of Se did not prevent island formation. This growth trend suggests that the supersaturation of Se in the chamber was in fact inhibiting the island formation of In-Se compounds. Fig.3.3 shows a successful $In2Se3$ growth on HOPG, with height profiles of various islands. After the reintroduction of a low Se background pressure, there is a population of slightly shorter islands with a less regular shape. Irregular, shorter islands are consistently observed across different growths of various heights, which will be discussed throughout the rest of this thesis.

Fig3.4 shows STM images of a taller island on the same sample, that shows both the AFE stripe characteristic of $\beta' - In_2Se_3$ and the FE zigzag feature characteristic of $\beta^* - In_2Se_3$. This verifies that the supplemental Se during the growth allowed for the formation of In_2Se_3 structures. Since our STM operates at 77K, the material is able to condense into both phases. There are several FE

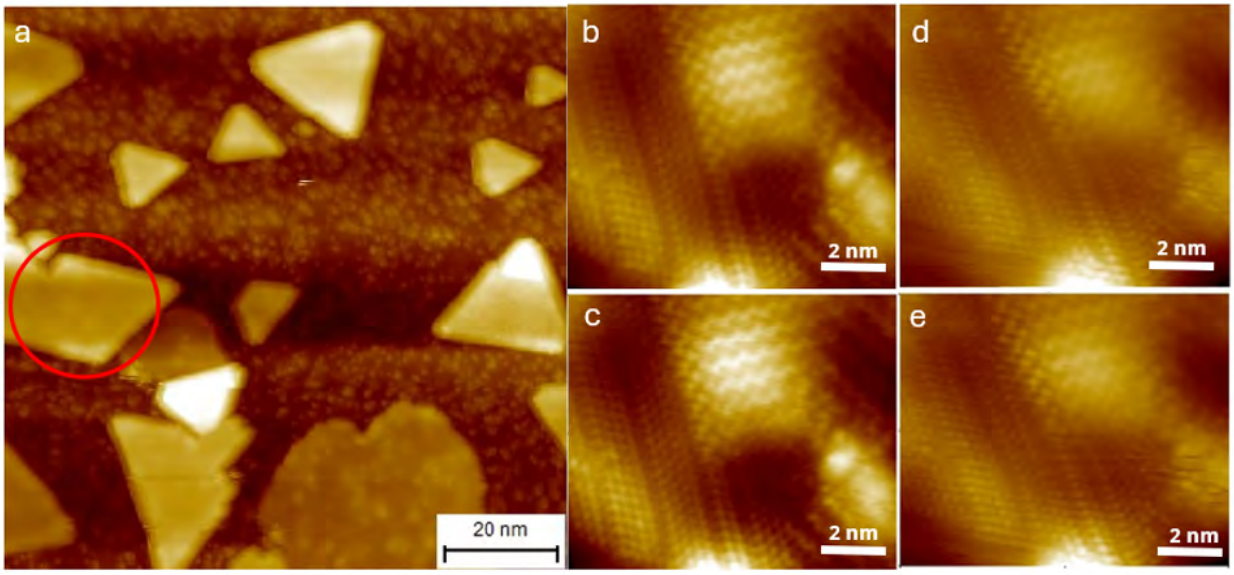

Figure 3.4 AFE and FE Stripe Features on In_2Se_3 Island a.) Large scale image of the surface. The red circle indicates the island shown in the zoomed in images, b.) and c.) are trace and retrace images taken simultaneously, d.) and e.) are trace and retrace images taken simultaneously. Scanning conditions: a.) 2V, 5pA, b.) and c.) 2V, 50pA, d.) and e.) 1.4V, 80pA.

domains present within the same island, suggesting some interruption to long-range FE ordering. Island height is an important fact to consider, since the FE properties of In_2Se_3 are attributed to broken symmetries within the 5-layer structure of material. Despite the rougher, irregular islands, the production of smooth In_2Se_3 islands with FE features bode well for future heterostructure samples and heterostructure samples were subsequently produced.

Several samples gave insight into specific aspects of the growth. Each sample described below uses an HOPG substrate and will be referred to by a sample number to distinguish between separate sample growths. The In_2Se_3 depositions on these samples were all conducted with the low Se background pressure established in the previous growths. Based on the sample growths described above, the irregularly shaped islands are most likely some derivative structure of In_2Se_3. The irregularly-shaped islands seem to be intrinsic to the grow process, since they were present on the surface during depositions with some Se background pressure, and not present during depositions with no Se background pressure, unless they were already present on the surface. These islands range in height, the shortest of which are ~5-6Å and the tallest of which are ~8-9Å. Several

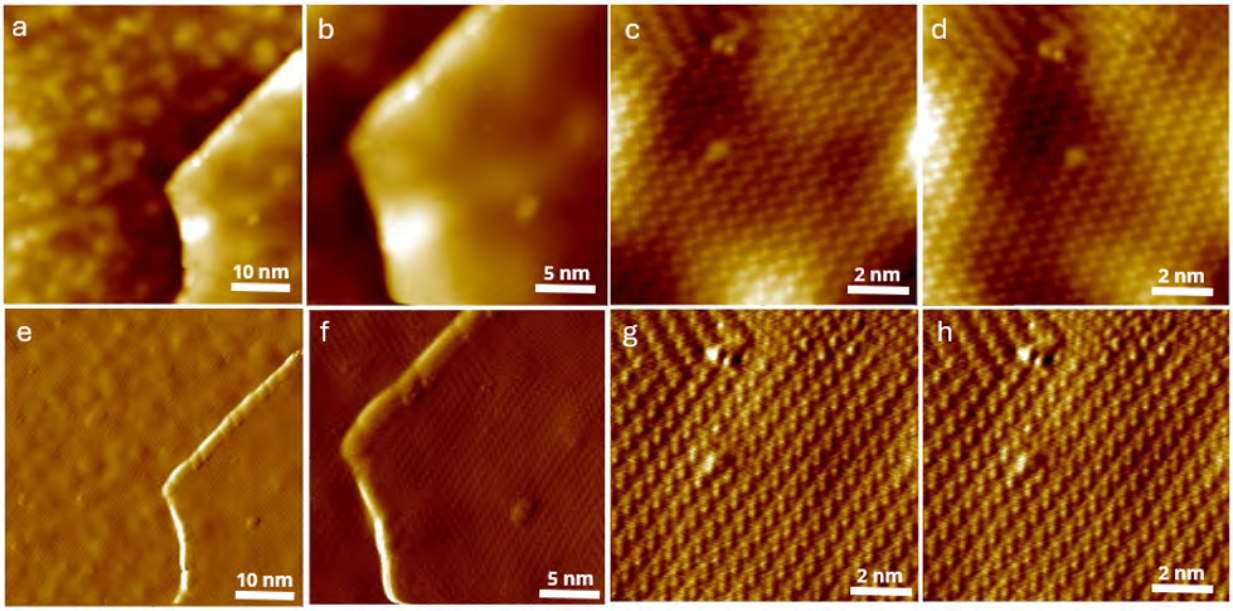

Figure 3.5 Sample 13 In_2Se_3 on $NbSe_2$/HOPG A region with multiple layers of In_2Se_3 is shown, where FE stripe features intrinsic to $\beta^* - In_2Se_3$ are visible on both layers. a.) – d.) are STM topography images and e.) – h.) are their corresponding current maps. Scanning conditions: a.) and e.) 2V, 5pA, b.) and f.) 2V, 5pA, c.) and g.) 2V, 50pA, d.) and h.) 2V, 50pA.

samples described below have taller irregular-shaped islands that exhibit In_2Se_3 FE stripe features, validating that these are in fact 5-layer In_2Se_3. This leads to the conclusion that the island shape is not necessarily an indicator for the island quality of In_2Se_3, and the shortest irregularly-shaped islands are an intermediate step in the formation of In_2Se_3 islands.

Sample 13 was the first attempt at a heterostructure sample after the optimization of the In_2Se_3 growth. It had a high coverage of $NbSe_2$ grown at a lower temperature to promote the formation of both the H and T phases. The goal was to study the vertical heterostructure between In_2Se_3 and $NbSe_2$, so a sufficiently large layer of $NbSe_2$ was required to allow for the formation of large In_2Se_3 islands on top. The growth rate of In_2Se_3 was higher than expected, and the sample had multiple layers of In_2Se_3. This is likely due to the different interactions between In_2Se_3 and $NbSe_2$ versus that with HOPG. Fig.3.5 shows a region with a rougher first layer and smoother second layer, both of which have $\beta^* - In_2Se_3$ zigzag features. This could indicate that there is a preference for the β^* phase on $NbSe_2$. Fig.3.6 shows two different regions of In_2Se_3 that have many FE domains, which seem to be disrupted by the roughness and defects within the film. Sample 13 would inform the

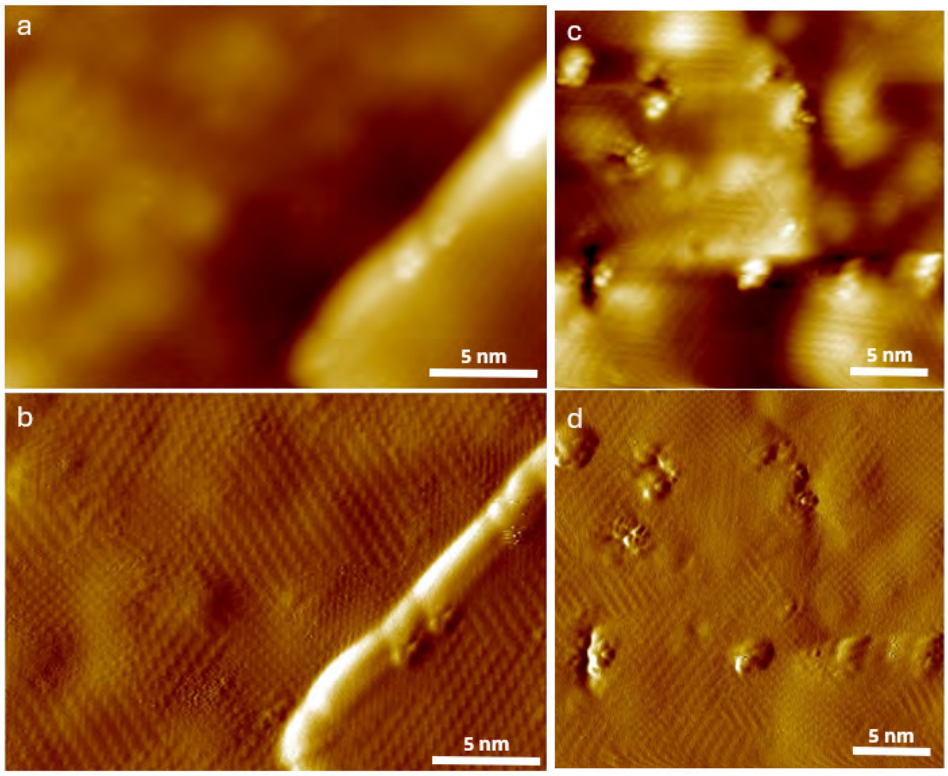

Figure 3.6 Sample 13 Many FE Domains in In_2Se_3 Corresponding topography images and current maps showing many difference FE domains within different regions of the film. Scanning conditions: a.) and b.) 2V, 10pA, c.) and d.) 2V, 5pA.

growth conditions for two future samples. The higher coverage of In_2Se_3 motivated the study of a high coverage of In_2Se_3 on HOPG, to verify if the preference for $\beta^* - In_2Se_3$ was consistent between samples. The high coverage of Sample 13 didn't allow for the formation of lateral heterostructures, which would need to be studied in a future sample.

Sample 16 was an attempt at a high coverage In_2Se_3/HOPG sample and therefore had a significantly longer deposition time compared to other samples. Sample 16 and 13 had the same growth parameters, except the deposition time for sample 16 was twice as long. Despite this increase, the coverage of sample 16 was lower than sample 13, indicating a large difference between the interaction between In_2Se_3 and $NbSe_2$ versus HOPG. Specifically, the sticking coefficient on $NbSe_2$ is higher than HOPG. Another important observation is that the properties of islands present on the surface varies by height. Fig.3.7 shows two islands on Sample 16 of various heights. The shorter island, described in Fig.3.7a-c, is disordered, rough, and lacks any overall crystallinity. The

taller island, described in Fig.3.7d-h, has a crystalline structure, visible in the FFT image Fig.3.7g of Fig.3.7f, which was then isolated to create the inverse FFT image Fig.3.7h. The taller island is most likely $\alpha - In_2Se_3$, since it is tall enough to be a 5-layer In_2Se_3 structure, but doesn't show signs of the intrinsic stripe features of either FE β phase. The shorter island further validates the hypothesis that the growth of In_2Se_3 has a

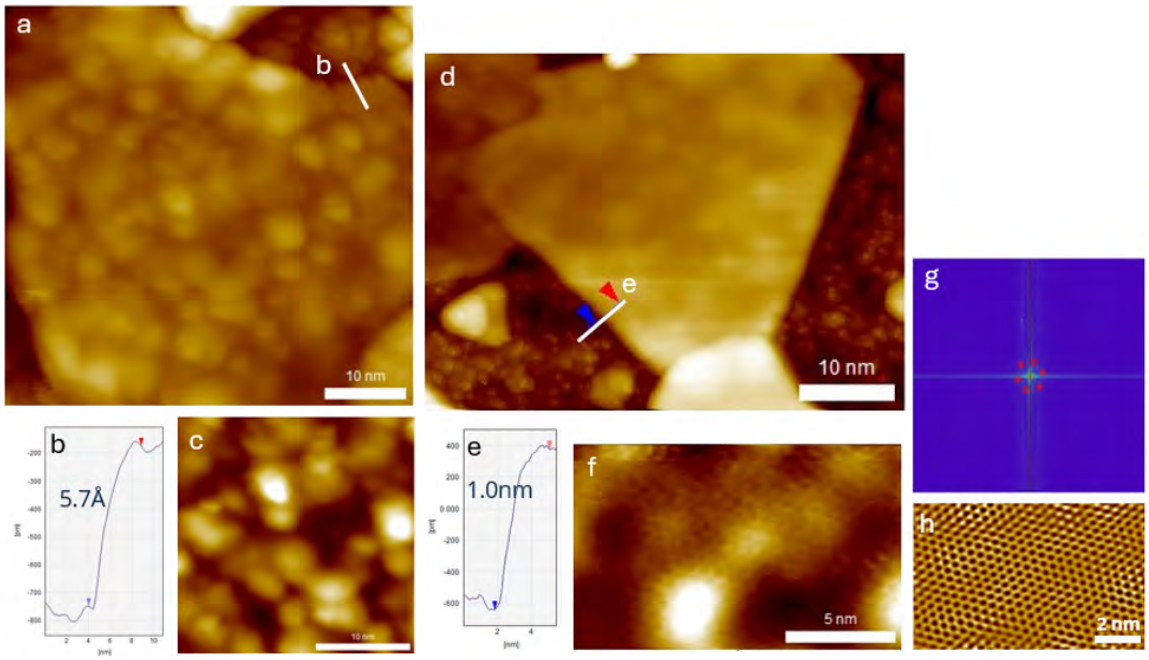

Figure 3.7 Sample 16 Island Height and Crystallinity in In_2Se_3 on HOPG a.) A short amorphous In_2Se_3 island, with a corresponding height profile shown in b.), c.) Zoomed in image of the island in a.), d.) In_2Se_3 island with a corresponding height profile shown in e.) and an image of the island in f.), g.) FFT image of f.), h.) inverse FFT image of g.). Scanning conditions: a.) 2V, 5pA, c.) 2V, 20pA, d.) 2V, 10pA, f.) 2V, 20pA.

Sample 14 had a lower coverage of $NbSe_2$ than Sample 13, to encourage the formation of lateral heterostructures of $In_2Se_3/NbSe_2$. Fig.3.8 shows a T-$NbSe_2$ island, with a prominent CDW feature visible in the island. There are several bumps within the island, likely larger clusters underneath the island, that do not significantly disrupt the CDW periodicity. There are some clusters present on the exposed HOPG surface. Island shape and height were used to differentiate between materials after the In_2Se_3 deposition, shown in Fig.3.9. Additionally, the cluster density on the surface is much higher and the roughness of $NbSe_2$ islands increased. The In_2Se_3 islands are irregular in shape

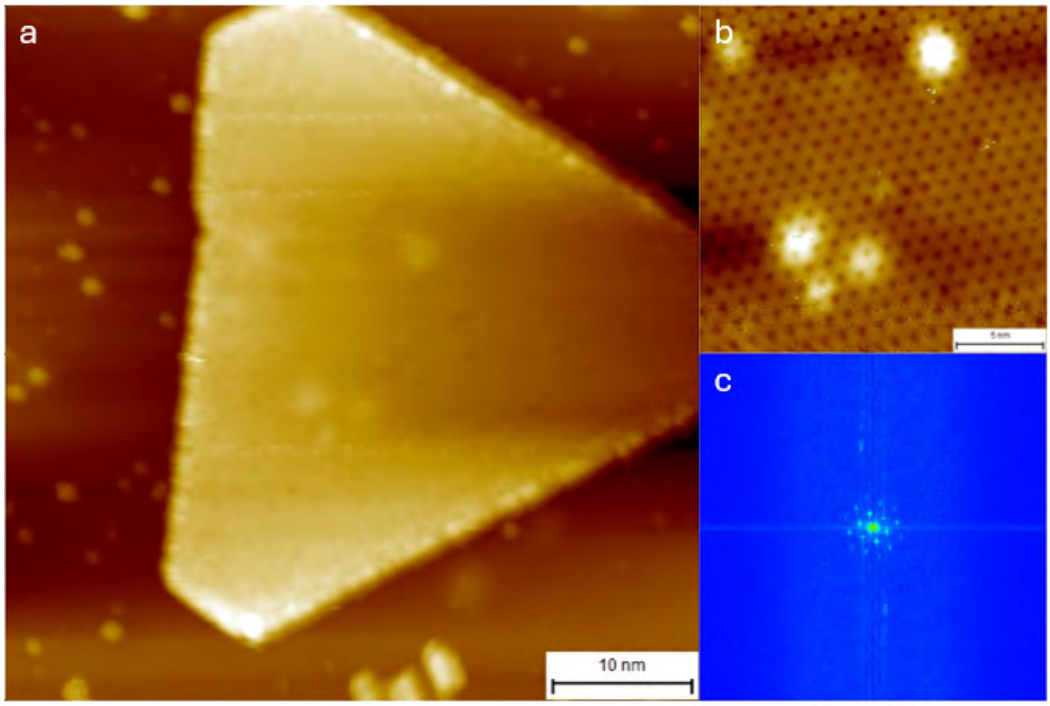

Figure 3.8 Sample 14 $NbSe_2$ on HOPG a.) A T-$NbSe_2$ island on bare HOPG, b.) Zoomed in image of the island in a.), showing the CDW, c.) FFT image of b.). Scanning conditions: a.) 2V, 10pA, b.) 2V, 50pA.

and nucleate at the edges of the $NbSe_2$ islands, suggesting that the island edges are energetically favorable places for the In-Se to nucleate. Despite the rough surface morphology for both materials, electronic features like the β' and β^* FE features and a Moiré pattern between $NbSe_2$ and In_2Se_3 are present.

Sample 18 was the final heterostructure sample grown and is the most extensively studied sample due to the quality of islands and the variety of structures observed. The substrate temperature used was on the higher end of the range used for our samples, to ensure there was a population of T-$NbSe_2$ on the sample. Fig.3.10 shows some example images of structures on the surface after the $NbSe_2$ deposition Fig.3.10a,b and after the In_2Se_3 deposition Fig.3.10c,d. There is a higher concentration of small clusters on the surface after the In_2Se3, as compared to the surface with $NbSe_2$. The smaller $NbSe_2$ islands tend to be T-$NbSe_2$, while the larger islands are H-$NbSe_2$, which make up a large percentage of the $NbSe_2$ islands seen on this sample. The H-$NbSe_2$ islands are large enough to allow for similarly large In_2Se_3 islands to form on top, while still leaving

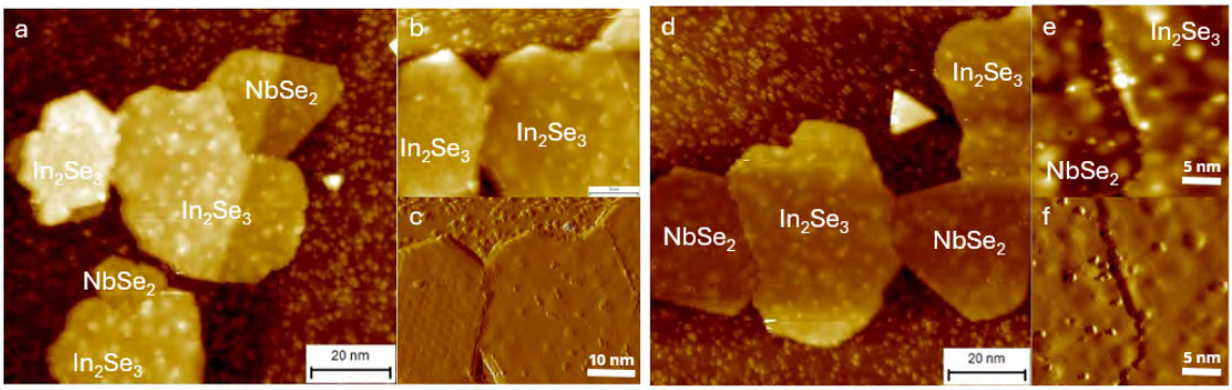

Figure 3.9 Sample 14 In_2Se_3 on $NbSe_2$/HOPG a.) Several In_2Se_3 islands growing on the edges of $NbSe_2$, with one island growing on top of an $NbSe_2$ island, b.) Zoomed in image of the vertical heterostructure and first layer In_2Se_3 boundary and the corresponding current map in c.), d.) In_2Se_3 lateral heterostructures with $NbSe_2$, e.) Zoomed in image of the boundary between materials and the corresponding current map in f.). Scanning conditions: a.) 2V, 5pA, b.) and c.) 2V, 10pA, d.) 2V, 5pA, e.) and f.) 2V, 5pA.

bare HOPG to allow for the formation of lateral heterostructures. Similar growth parameters as previous depositions were used for the In_2Se_3, though the growth was shorter since the growth rate on $NbSe_2$ is higher than HOPG and we didn't want to fully cover the $NbSe_2$ layer like Sample 13. The next section of this chapter will explore the different structures on Sample 18 and their properties.

3.3 Short In_2Se_3 Islands

3.3.1 Comparing 3-layer and 5-layer Islands

As discussed in the previous section, $In2Se3$ islands with various properties have been observed on the samples studied. One species of islands is in vertical heterostructures with $NbSe2$. These are shorter than the expected apparent heights for $In2Se3$, which has five atomic layers. Comparing the height of $In2Se3$ islands directly on HOPG versus those on $NbSe2$, as shown in Fig.3.11, the apparent height of the shorter islands is between ~5-7Å while the taller islands are over 8Å. Since the taller islands typically show the FE stripe features of β' and $\beta^* - In_2Se_3$, we can use these as the basis for our height analysis. There is some variation in the heights of islands, which could be due to the STM tip condition, varying electronic DOS, and imprecision in the line profiles taken on each image. The short In_2Se_3, however, are comparable in height to $NbSe_2$, which has 3 atomic

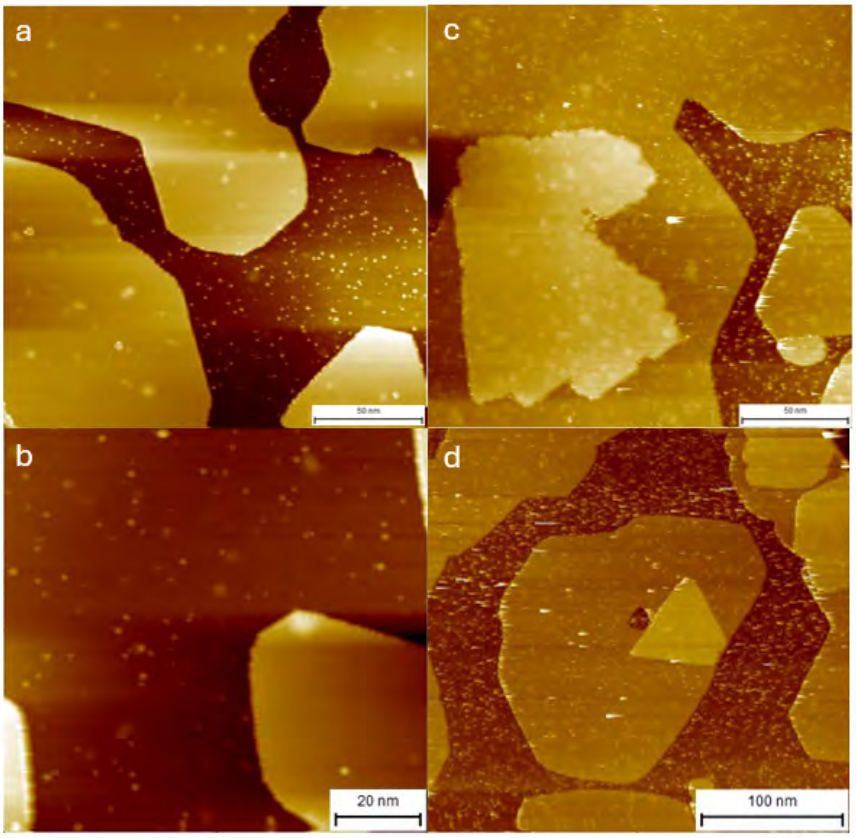

Figure 3.10 Sample 18 In_2Se_3 and $NbSe_2$ Heterostructure on HOPG a.) and b.) show the initial $NbSe_2$ growth, c.) and d.) show the sample after the In_2Se_3 deposition. Scanning conditions: a.) -2V, 20pA, b.) 2V, 10pA, c.) 2.2V, 5pA, d.) 2V, 5pA.

layers as compared to the 5-layer In_2Se_3.

The difference between the growth of In_2Se_3 on $NbSe_2$ versus HOPG indicates differences in the interactions between these materials. The growth rate on $NbSe_2$ is higher than that on HOPG, and there is a difference in the structure of islands on each material. Fig.3.12 shows In_2Se_3 islands of similar heights, ~5-6Å, on bare HOPG and $NbSe_2$, in Fig.3.12a,b and Fig.3.12c,d, respectively. The islands grown on HOPG are amorphous and rough, as opposed to the crystalline islands grown on $NbSe_2$. It seems that due to the interactions between $NbSe_2$ and In_2Se_3, a partial structure of In_2Se_3 is stabilized. The partial structure is likely composed of 3 atomic layers, since it is similar in height to $NbSe_2$ and comparable partial structures are reported in the literature.

Chen et al. studied the growth process of $\beta - In_2Se_3$, showing partially formed In_2Se_3 islands ranging from a single atomic layer to the full five-layer structure [23]. They used a gold substrate

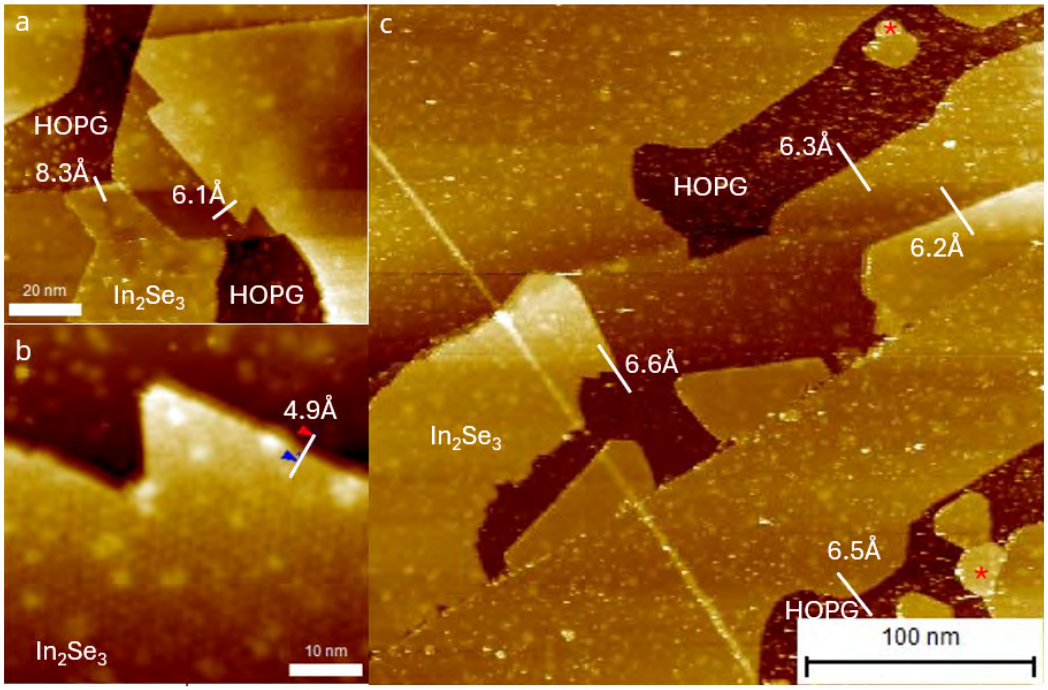

Figure 3.11 Height Comparisons of In_2Se_3 and $NbSe_2$ Heterostructure on HOPG In_2Se_3 islands in all images are labeled with text or a red star. All other structures are $NbSe_2$. The white lines indicate a line profile taken at that point, with the measured height adjacent to it. a.) has a region of In_2Se_3 on bare HOPG, while In_2Se_3 in b.) and c.) in on top of $NbSe_2$. The scanning conditions for each image is as follows: a.) -2V, 5pA; b.) 2V, 10pA; c.) 2V, 5pA.

because it bonds strongly to In_2Se_3. Our growths have suggested that there are strong interactions between In_2Se_3 and $NbSe_2$, with indicators such as the higher sticking coefficient and faster growth rate. It is likely that the interactions of these materials also have the ability to stabilize a partial structure growth. It has been reported that $NbSe_2$ can bond with and stabilize a metastable In-Se based structure, $InSe_2$ [35]. This strong interaction could be an intrinsic property of this material system.

STS curves from two different short In_2Se_3 islands are shown in Fig.3.13, with Fig.3.13a-c showing curves taken in the center of an island exhibiting a Moiré pattern. Key points along a line STS are shown for comparison purposes, and the entire line STS will be discussed in greater detail below. Fig.3.13d-f show curves taken from the edge on the island inward. The curves are taken at different scanning conditions, varying the height of the STM tip. Both curves have a feature between $0.25V$ and $0.5V$, which gets stronger moving towards the interior of the islands. It is

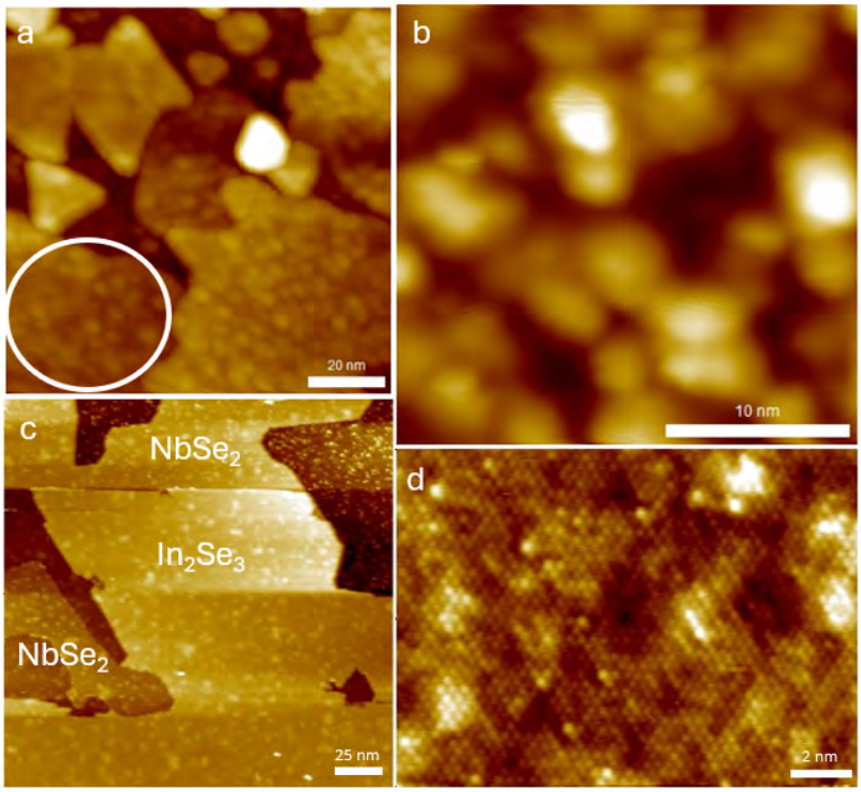

Figure 3.12 Crystallinity of Short In_2Se_3 Islands a.) and b.) are In_2Se_3 islands on HOPG. The specific area measured is circled in a.), c.) and d.) are In_2Se_3 islands on $NbSe_2$. Scanning conditions: a.) 2V, 5pA, b.) 2V, 20pA, c.) 2V, 5pA, d.) -1V, 50pA.

unclear if this feature is an in-gap state or if it marks the beginning of the rise of the CB The curves vary significantly in the negative part of the spectrum, corresponding to the valence band side of the material's electronic spectrum. Several curves have a VB rise of about $-0.75V$, while the others have a much shallower rise and it is difficult to define a precise band edge. Another variable feature is at $-1.1V$, varying in strength and precise location in Fig.3.13f and only appearing in one curve in Fig.3.13c. These variations indicate that the interactions between In_2Se_3 and $NbSe_2$ strongly affect the electronic properties of the VB, as opposed to the CB.

For comparison purposes, Fig.3.14 shows line STS curves of a lateral heterostructure boundary between T-$NbSe_2$ and In_2Se_3. The entire line STS is discussed in section 3.4.4, but here the In_2Se_3 side of the boundary is useful for the identification of the shorter islands. There are notable differences between the curves, on both the CB and VB sides of the spectrum. Closer to the boundary, the VB starts to rise much earlier, suggesting an influence on the band structure from

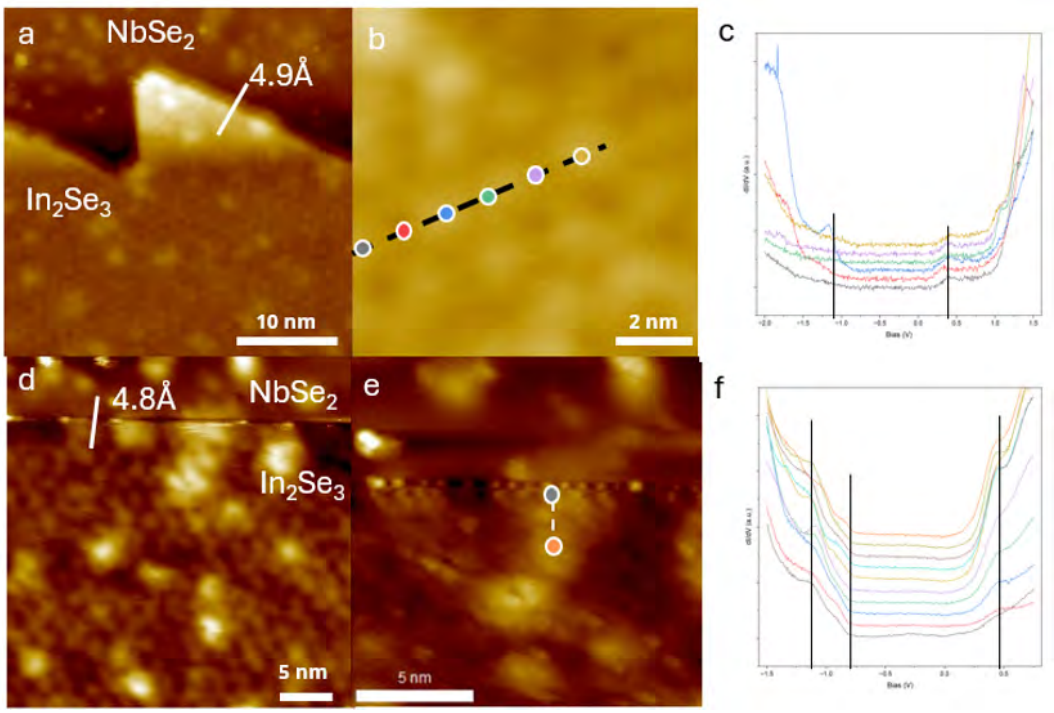

Figure 3.13 Moiré Pattern STS a.) and d.) are two different In_2Se_3 islands on $NbSe_2$ with the height of the island labeled in each image, b.) Zoomed in image of a.) with key points along a line STS marked with circles corresponding to the colors in c.), e.) Zoomed in image of d.) with line STS moving away from the island edge, shown in f.). Scanning conditions: a.) 2V, 10pA, b.) 1.2V, 50pA, d.) 2V, 20pA, e.) -1.1V, 20pA. STS curves were taken at (c) 1.2V, 50pA and (f) -1.1V, 100pA and the curves are offset to show detail.

$NbSe_2$. The exact character of these features are unclear and requires further study. The bandgaps in Fig.3.13 and Fig.3.14 seem to have a significant difference, indicating that the shorter islands may be $\alpha - In_2Se_3$.

3.3.2 Properties of the Moiré Pattern

A preliminary study of the Moiré pattern between In_2Se_3 and $NbSe_2$ is presented. Fig.3.15 shows a region of In_2Se_3 on $NbSe_2$, exhibiting a Moiré pattern with location dependent electronic properties in the STS curves. While there are variations in peak intensity in the conduction band, there are several curves with significantly higher DOS and extra peaks in the valence band. Different regions in the Moiré pattern should have slightly different interactions with the layer underneath due to differences in the stacking of atoms, which would therefore change the electronic properties of the respective region. Shabani et al. discussed the different stacking configurations possible in

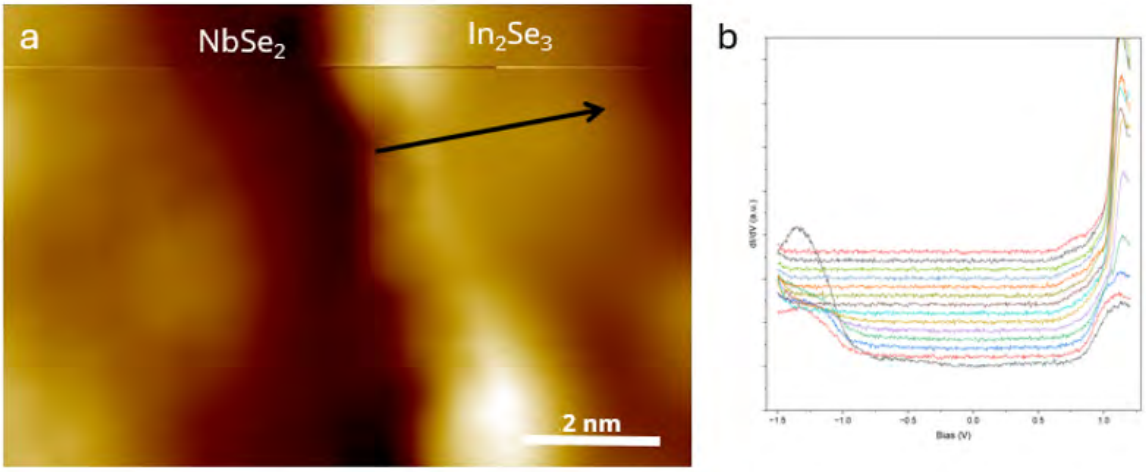

Figure 3.14 In_2Se_3 STS a.) Boundary between $NbSe_2$ and In_2Se_3 with a black arrow indicating line STS moving away from the boundary, shown in b.). Scanning conditions: a.) 2V, 20pA. STS curves taken at 1V, 20pA and curves are offset to show detail.

TMD systems, which should be similar to our case due to the formation of short In_2Se_3 islands [48]. As previously mentioned, there is a consistent peak at $0.5V$ with more variations in the VB side of the spectrum. Since the features at $-1.1V$ and $-1.8V$ are not present in all curves, they are likely electronic variations due the stacking differences in the Moiré pattern.

3.4 Tall In_2Se_3 Islands

3.4.1 5-layer Islands

The apparent height of islands is an important indicator in identifying what material they are composed of, since the 5-layer In_2Se_3 islands are notably taller than other materials. They are also identifiable by the characteristic stripe features of β' and β^* phase In_2Se_3, which are both observable at LN2 temperature. Fig.3.16 shows examples of the structures seen on Sample 18. Most of the tall islands are in some form of lateral heterostructure, shown in FIGURE B, growing directly on HOPG and at the edge of an $NbSe_2$ island. It seems more energetically favorable for the In_2Se_3 to form on the edges since it conforms to the gaps between the $NbSe_2$. Very few tall islands found on top of $NbSe_2$ like in Fig.3.16a, and those that are grow laterally to second-layer $NbSe_2$ islands which seem to stabilize them. The few islands of this type that were observed were fragile and were destroyed by the STM tip.

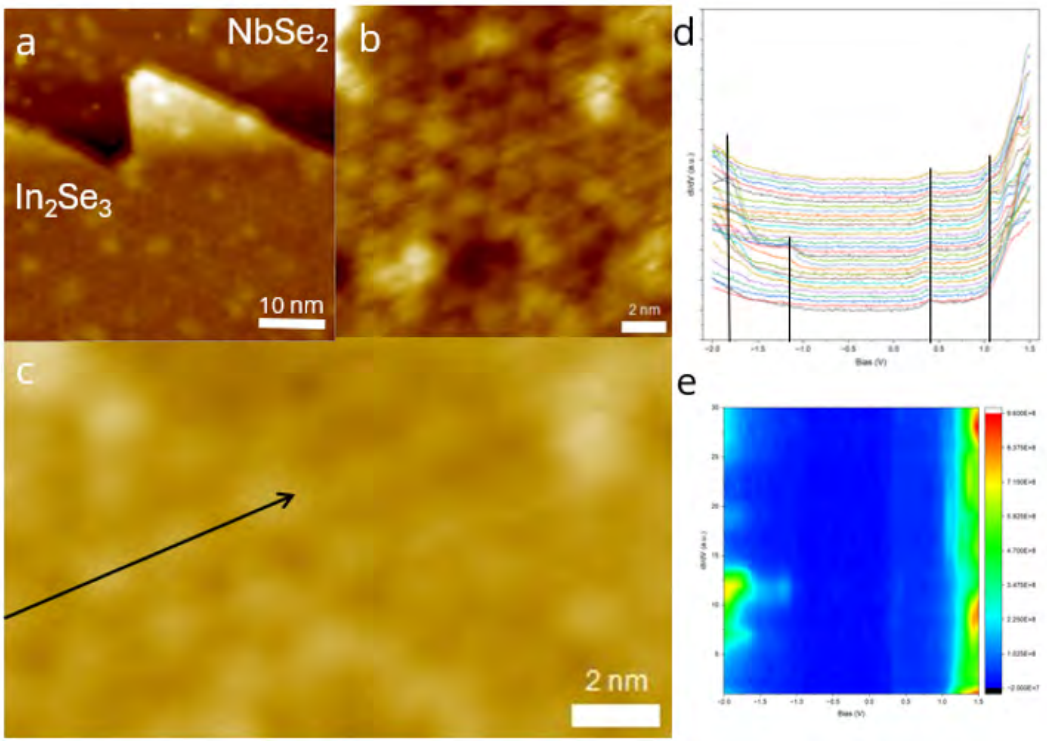

Figure 3.15 Moiré Pattern STS a.) In_2Se_3 island on $NbSe_2$, b.) Moiré pattern between the two materials, c.) Line STS indicated by the black arrow, with corresponding curves and waterfall plot shown in d.) and e.). Scanning conditions: a.) 2V, 10pA, b.) 0.8V, 50pA, c.) 1.2V, 50pA. STS curves were taken at 1.2V, 50pA and the curves are offset to show detail.

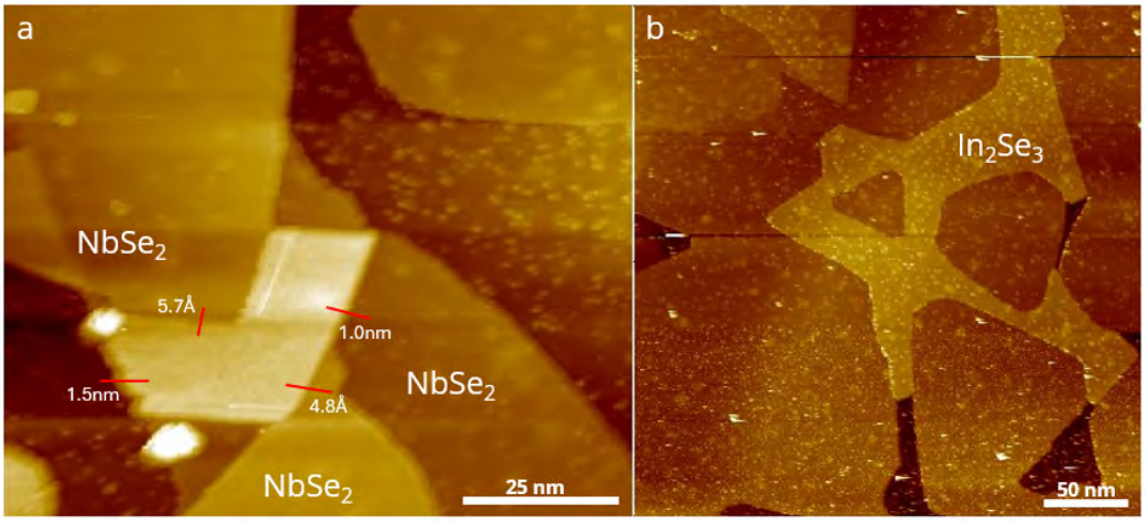

Figure 3.16 Examples of Tall In_2Se_3 Structures a.) In_2Se_3 island on $NbSe_2$, wedged between two second layer $NbSe_2$ islands. The red lines represent line profiles with their corresponding height measurements next to them, b.) Core-shell structure, due to In_2Se_3 conforming to the spaces in between $NbSe_2$ islands. Scanning Conditions: a.) 2.5V, 5pA, b.) 2V, 5pA.

3.4.2 Fragile Vertical Heterostructures

The tall islands observed on top of $NbSe_2$ are very uncommon and therefore difficult to study. The position of these islands, on top of first-layer $NbSe_2$ and laterally to second-layer $NbSe_2$, was uncommon for all In_2Se_3 islands on Sample 18, likely due to the low coverage of second-layer $NbSe_2$. Since most of the tall In_2Se_3 islands grew laterally to $NbSe_2$ islands, conforming to the gaps between islands, the nucleation of In_2Se_3 islands on $NbSe_2$ edges could allow for the formation of these structures, although they are very uncommon. Fig.3.18a-c shows the interesting stripe features on the surface of these islands, which is reminiscent of the $\beta' - In2Se3$ stripe feature. The stripe is several atoms thick with high intensity and low intensity regions but does not share the clear AFE character of alternating slanting of the stripes. There are also several different stripe directions, which are likely the different domains of the electronic feature.

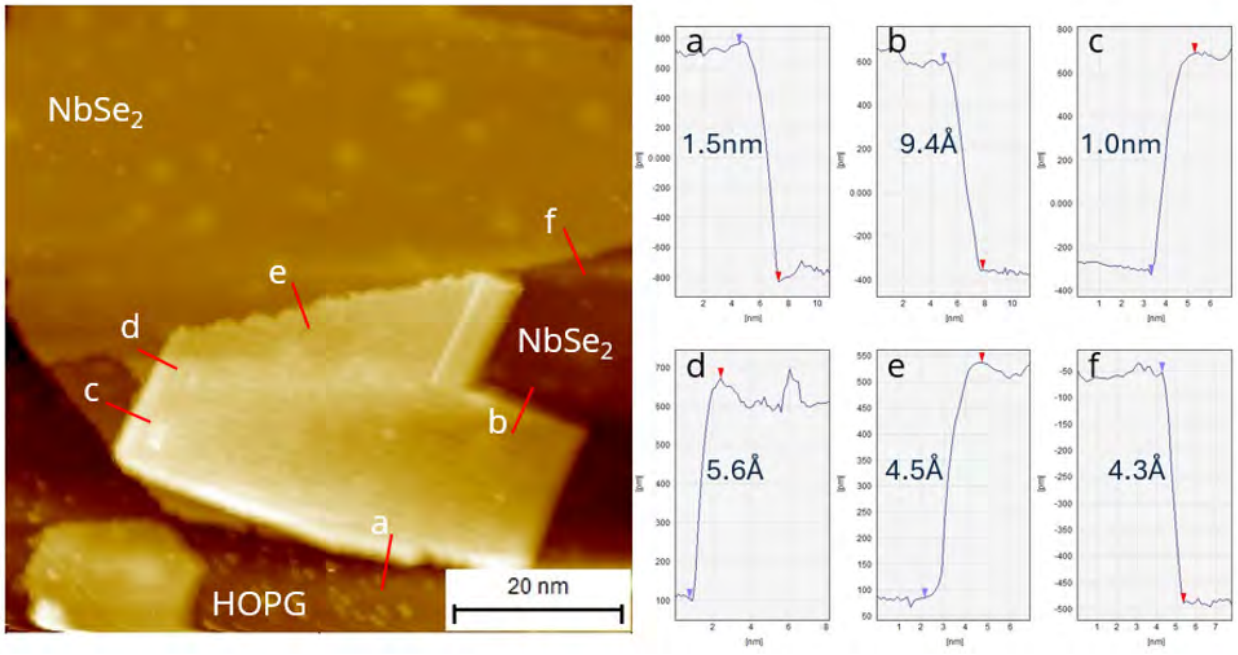

Figure 3.17 Tall In_2Se_3 and $NbSe_2$ Heterostructure on HOPG Various height profiles measuring the island and surrounding features. Scanning Conditions: 2V, 5pA.

Both islands of this type that were found were subsequently destroyed by the STM tip during scanning, indicating that they are unstable. Fig.3.18d shows the crater formed in one island, and the other island was destroyed in a similar fashion. The islands essentially decomposed because

of the interaction between it and the STM tip, which forms an electric field between the sample of varying strength depending on the bias voltage. This decomposition is interesting, considering Sample 13, which had a high coverage of In_2Se_3 on top of a full monolayer of $NbSe_2$. Additionally, the stability of other In_2Se_3 islands has not been an issue. This suggests that at lower coverage, the shorter islands are more favorable for vertical heterostructures with $NbSe_2$.

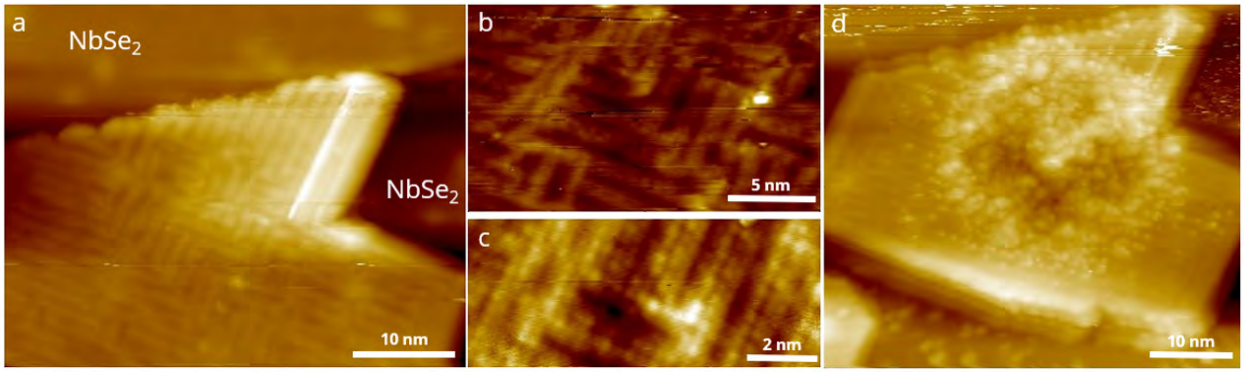

Figure 3.18 Tall In_2Se_3 and $NbSe_2$ Heterostructure Features a.) In_2Se_3 island with interesting stripe features, formed on an $NbSe_2$ and laterally next to an $NbSe_2$ island that is either a second layer island on is on a higher HOPG step, b.) and c.) show zoomed in images of the stripe features, d.) The same island after being destroyed by the STM tip. Scanning conditions: a.) and b.) 2V, 20pA, c.) 1.5V, 50pA, d.) 2.5V, 5pA.

3.4.3 Stable Lateral Heterostructures

A vast majority of tall In_2Se_3 islands grew on bare HOPG, laterally to $NbSe_2$ islands. The physical boundaries between the materials have a significant height difference, since $NbSe_2$ is composed of 3 atomic layers versus the 5-layer In_2Se_3 structure. Fig.3.19 shows several boundaries between $NbSe_2$ and In_2Se_3, which has bumpy features along the edge of the In_2Se_3 island. In Fig.3.19b, two small regions of $\beta^* - In_2Se_3$ are surrounded by regions without any obvious FE ordering, which separate the β^* from the island edge. This could indicate a disruption in the FE ordering due to either electronic interactions with the $NbSe_2$ or a shift in the atomic structure of the crystal, since the central Se layer is responsible for the FE polarization in In_2Se_3. Above the boundary, there is a slight indication of the T-$NbSe_2$ CDW. Fig.3.19c,d show either side of a boundary, since the height difference between the islands make it difficult to get resolution of features of each side simultaneously. The T-$NbSe_2$ CDW, shown in Fig.3.19c, survives very close

to the boundary, which aligns with the robust nature of the CDW reported in the literature. In Fig.3.19d, several $\beta' - In2Se3$ domains, which seem to avoid a particularly large bright feature that looks like a collection of atoms nucleating on the edge of the island, based on the resolution. The β' stripes also survive very close to the edge, raising questions about the interaction between T-$NbSe_2$ and β' vs β^*. Another example of the FE ordering at the boundary is shown below.

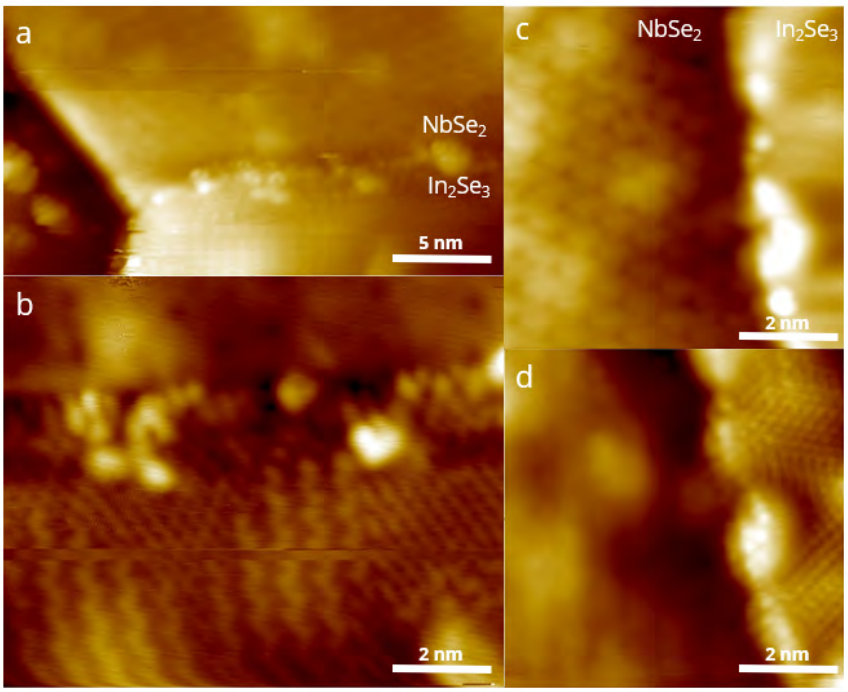

Figure 3.19 $In_2Se_3/NbSe_2$ Boundaries a.) and b.) are images of the same pair of islands, and c.) and d.) are another pair of islands. Scanning conditions: a.) and b.) 2V, 5pA, c.) 2V, 20pA, d.) 1V, 750pA.

A special type of lateral heterostructure is a core-shell structure, in which one material fully surrounds the other. Similar to other heterostructures, fairly smooth boundary with some atoms along the edges and bright features. The shape of the $NbSe_2$ island in the center of the structure is typical for a T-phase island, although no CDW was observed which indicates that the island is H-$NbSe_2$. It's possible that In_2Se_3 fully surrounding the interior island could influence the phase of $NbSe_2$, similar to [47], though further study is required. The β' stripe in Fig.3.20c survives to the edge of the boundary and there are faint signatures of the β^* zigzag stripe, but there are also regions at the boundary with no obvious FE ordering. The physical properties of the boundary

could determine whether FE polarization can survive, since there are varying amounts of atoms nucleating on different regions of the boundary.

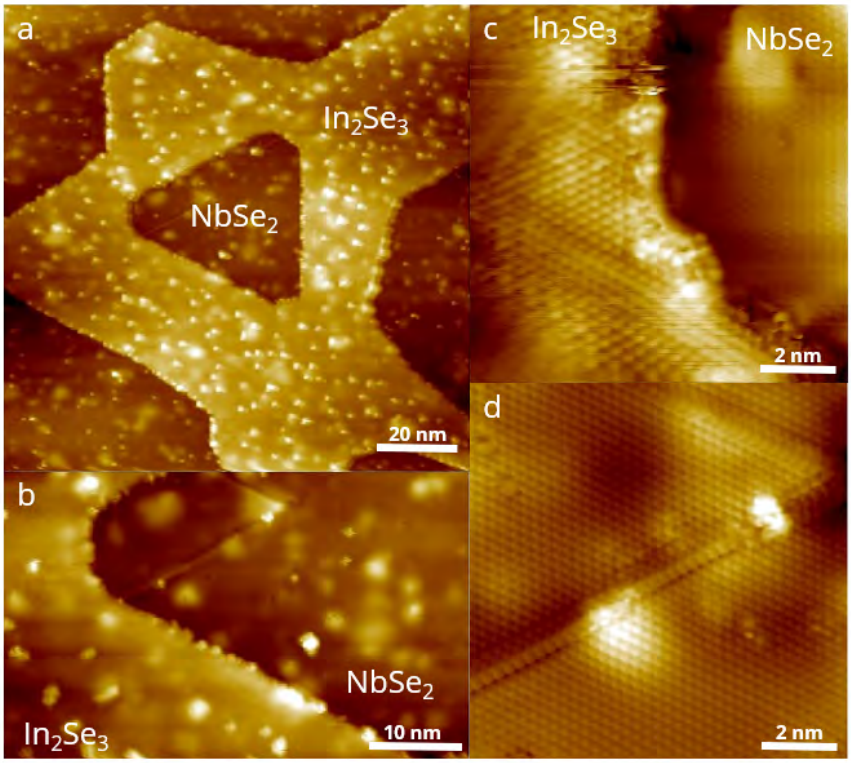

Figure 3.20 $In_2Se_3/NbSe_2$ Core-Shell Structure a.) Large scale image showing In_2Se_3 growing in between $NbSe_2$ fully surrounding one island, b.) Zoomed in image of one boundary of the core-shell structure. A triangular domain of $NbSe_2$ is the area shown in d.), c.) Image of the boundary, with some FE features in the In_2Se_3. Scanning conditions: a.) 2V, 5pA, b.) 2V, 10pA, c.) 1.4V, 40pA, d.) -1.2V, 50pA.

3.4.4 Properties of Lateral Heterostructures

The boundary between materials in lateral heterostructures can give insight into the interactions between the materials, and the preliminary results of an STS study of the boundary are presented here. Fig.3.21 shows line STS curves taken across the boundary between T-$NbSe_2$ and $\beta' - In2Se3$ indicated by the black arrow. The entire line STS is shown in Fig.3.21b,c and the region of the line indicated by the white lines is shown in Fig.3.21d,e to show details. Because of the differences in electronic structure of each material, the STS voltage range was limited, specifically on the valance band side where the band edge of In_2Se_3 is not visible. There is a high DOS at the boundary,

indicating a potential boundary state. On the T-$NbSe_2$ side, the valence band peaks in each curve shift away from the Fermi level approaching the boundary, while the conduction band peaks on the In_2Se_3 are dampened when approaching the boundary.

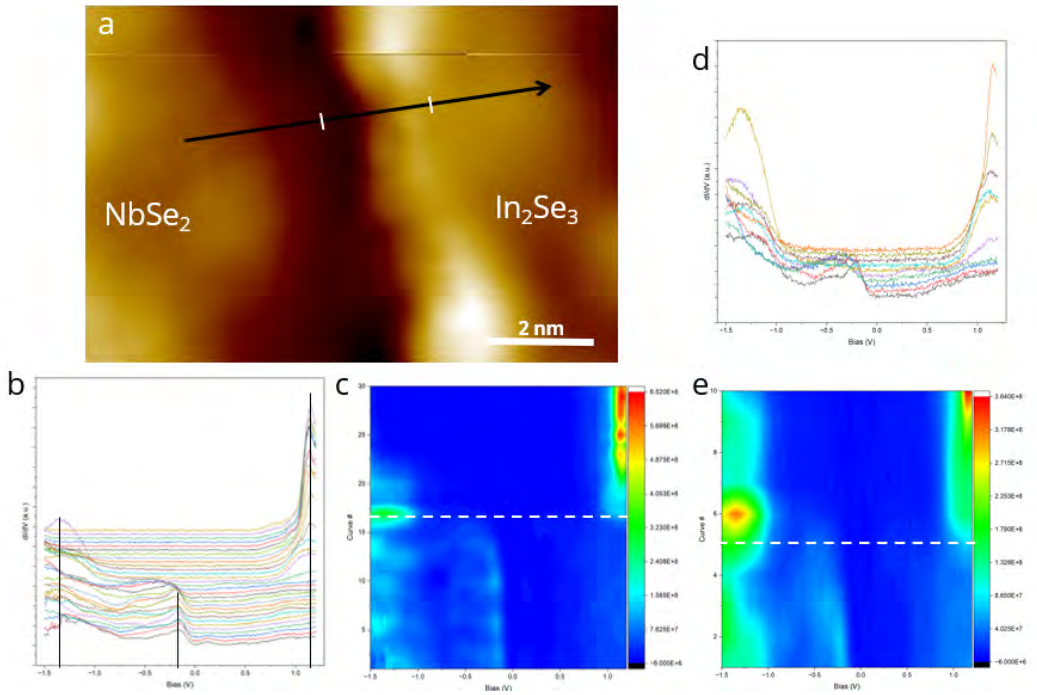

Figure 3.21 $In_2Se_3/NbSe_2$ Lateral Heterostructure a.) Interface between $NbSe_2$ and In_2Se_3, b.) and c.) are the curves and waterfall plot taken over the black arrow, d.) and e.) are select curves from the same line, between the white lines, to show detail in curves near the boundary. Scanning conditions: a.) 2V, 20pA. STS curves taken at 1V, 20pA and curves are offset to show detail.

STS curves were also taken at the boundary of the core-shell structure. In order to show the full shape of the In_2Se_3 band, line STS curves were taken on each material individually. Similar to Fig.3.21, Fig.3.22 shows a high density of states in the H-$NbSe_2$ curve closest to the boundary, as well as band bending in the valence band and the broadening of a peak in the conduction band moving away from the boundary. There are variations in the rise of the valance band as well as the intensity of the conduction band peaks in the In_2Se_3 STS, but no clear trends are present in this data set. Considering both sets of STS, there seems to be an influence on the electronic structure of $NbSe_2$ from interactions with In_2Se_3. A thorough study of these boundaries could help to understand the extent of this effect, since the T-$NbSe_2$ CDW seemed to survive at the boundary in

Fig.3.19.

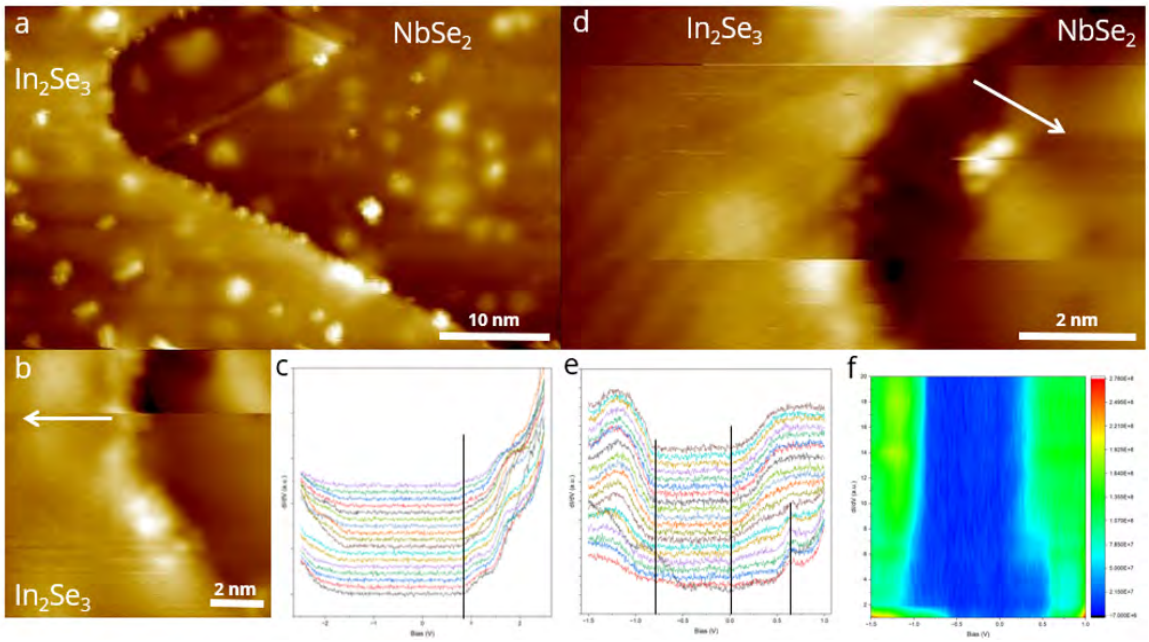

Figure 3.22 Core-Shell STS at Boundary a.) $In_2Se_3/NbSe_2$ boundary, b.) and c.) are the image and line STS on In_2Se_3 along the white arrow, d.) shows a different region of the boundary where line STS was taken on $NbSe_2$ along the white arrow, with corresponding curves and waterfall plot in e.) and f.). Scanning conditions: a.) 2V, 10pA, b.) and d.) 1.4V, 40pA. STS curves were taken at 1.4V, 20pA and are offset to show detail.

CHAPTER 4

CONCLUSION

In conclusion, we optimized the heterostructure growth for sub-monolayer coverage to study the interactions between In_2Se_3 and $NbSe_2$. The Se background pressure present during the deposition was an important parameter in determining the overall surface morphology. The presense of a Se background pressure affected the growth of islands, forming triangular islands and a shorter class of irregularly-shaped islands, some of which were 5-layer In_2Se_3 and some of which were are shorter partial structure of the material. The interactions between In_2Se_3 and $NbSe_2$ were stronger than that between In_2Se_3 and HOPG, as exhibited by several characteristics. The growth rate of In_2Se_3 was much higher on $NbSe_2$, and at high In_2Se_3 coverage there seemed to be a preference for the β^* phase. The strong interactions between the materials stabilize a 3-layer In_2Se_3 structure, which forms a Moiré pattern with the $NbSe_2$ underneath it. The Moiré pattern exhibits location dependent electronic features as seen in the STS curves. In_2Se_3 conformed to the $NbSe_2$ when growing laterally in relation to it, and STS curves show potential boundary states at the interface.

Future experiments could help us answer many remaining questions about this system. Theoretical models of the interactions between $NbSe_2$ and In_2Se_3 could determine the nature of these interactions and confirm the 3-layer structure hypothesis. Further experimental data is needed to fully understand the various phenomena proposed in this thesis. More thorough STS study of the Moiré pattern and the different regions of its unit cell, as well as at the boundary of the lateral heterostructures would reveal more about the electronic interactions between In_2Se_3 and $NbSe_2$. This STS study should include precise measurement of the VB and CB edges at locations throughout these systems. Low temperature measurements at LHe temperatures could also deepen our understanding of this system, since H-$NbSe_2$ has a low temperature CDW phase. Furthermore, $InSe$ was almost entirely overlooked in our experiments, and an $InSe/NbSe_2$ heterostructure study would continue to give insight into this material system and its interesting properties.

BIBLIOGRAPHY

[1]S. M. Girvin and K. Yang, *Modern condensed matter physics* (Cambridge University Press, 2019).

[2]H. Zhang, "Ultrathin two-dimensional nanomaterials", ACS Nano **9**, 9451–9469 (2015).

[3]C. Tan, X. Cao, Q. He, et al., "Recent advances in ultrathin two-dimensional nanomaterials", Chemical Reviews **117**, 6225–6331 (2017).

[4]R. Resta, "Modern theory of polarization in ferroelectrics", Ferroelectrics **117**, 6225–6331 (1994).

[5]H. Yamada, M. Marinova, P. Altuntas, et al., "Ferroelectric control of a mott insulator", Scientific Reports **3**, 2834 (2013).

[6]J. Chen, P. Cui, and Z. Zhang, "Ferroelectricity-tuned band topology and superconductivity in 2d materials and related heterostructures", Advanced Functional Materials **34**, 2408625 (2024).

[7]C. A. F. Vaz, Y. J. Shin, M. Bibes, et al., "Epitaxial ferroelectric interfacial devices", Applied Physics Reviews **8**, 041308 (2021).

[8]C. Kittel, *Introduction to solid state physics*, 8th ed. (Wiley, 2005).

[9]R. Fei, W. Kang, and L. Yang, "Ferroelectricity and phase transitions in monolayer group-iv monochalcogenides", Physical Review Letters **117**, 097601 (2016).

[10]S. Li, F. Wang, and Y. Wang, "Van der waals ferroelectrics: theories, materials, and device applications", Advanced Materials **36**, 2301472 (2023).

[11]A. Sarkar and E. Stratakis, "Recent advances in 2d metal monochalcogenides", Advanced Science **7**, 2001655 (2020).

[12]M. Yu, M. Hilse, and Q. Zhang, "Review of nanolayered post-transition metal monochalcogenides: synthesis, properties, and applications", ACS Applied Nano Materials **7**, 2800828026 (2024).

[13]C. Tan, W. Fu, and K. Loh, "Polymorphism and ferroelectricity in indium(iii) selenide", Chemical Reviews **123**, 87018717 (2023).

[14]W. Zhu, T. Low, H. Wang, et al., "Nanoscale electronic devices based on transition metal dichalcogenides", 2D Materials **6**, 032004 (2019).

[15]H. Ryu, K. Xu, D. Li, X. Hong, and W. Zhu, "Empowering 2d nanoelectronics via ferroelectricity", Applied Physics Letters **117**, 080503 (2020).

[16]Y. Li, C. Chen, W. Li, et al., "Orthogonal electric control of the out-of-plane field-effect in 2d ferroelectric $\alpha-$in2se3", Advanced Electronic Materials **6**, 2000061 (2020).

[17]D. Huo, Y. Bai, X. Lin, et al., "Visualizing interface states in $In_2Se_3 - WSe_2$ monolayer lateral heterostructures", Chinese Physics B **32**, 056803 (2023).

[18]D. Huo, Y. Bai, X. Lin, et al., "Tuning of the valley structures in monolayer $In2Se3/WSe2$ heterostructures via ferroelectricity", Nano Letters **22**, 7261–7267 (2022).

[19]J. He, T. Li, L. Zhang, et al., "Efficient energy transfer in $In2Se3\breve{}MoSe2$ van der waals heterostructures", ACS Omega **3**, 11930–11936 (2018).

[20]X. Huang, J. L. Lado, J. Sainio, P. Liljeroth, and S. C. Ganguli, "Doped mott phase and charge correlations in monolayer $1T-NbSe_2$", Phys. Rev. Lett. **134**, 046504 (2025).

[21]M. Liu, J. Leveillee, S. Lu, J. Yu, H. Kim, C. Tian, Y. Shi, K. Lai, C. Zhang, F. Giustino, and C.-K. Shih, "Monolayer 1t-nbse₂ as a 2d-correlated magnetic insulator", Science Advances **7**, eabi6339 (2021).

[22]S. M. Poh, S. J. R. Tan, H. Wang, P. Song, I. H. Abidi, X. Zhao, J. Dan, J. Chen, Z. Luo, S. J. Pennycook, A. H. Castro Neto, and K. P. Loh, "Molecular-beam epitaxy of two-dimensional In_2Se_3 and its giant electroresistance switching in ferroresistive memory junction", Nano Letters **18**, 6340–6346 (2018).

[23]Z. Chen, M. Sun, H. Li, et al., "Oscillatory order-disorder transition during layer-by-layer growth of indium selenide", Nano Letters **23**, 1077–1084 (2023).

[24]C. A. Voigt, M. Reingold, A. Dube, et al., "Molecular beam epitaxy synthesis of In_2Se_3 films", Journal of Vacuum Science and Technology A **42**, 032707 (2024).

[25]S.-K. Wu, H.-J. Wang, S.-W. Hsiao, J.-S. Huang, W.-C. Chou, C.-S. Yang, S.-J. Chang, C.-H. Wu, and Y.-C. Huang, "Control of lateral epitaxial nanothin β-in2se3 grown by molecular beam epitaxy: implications in fabricating of next-generation transistors", ACS Applied Nano Materials **7**, 20445–20453 (2024).

[26]H. Brune, *Epitaxial growth of thin films* (Wiley, 2014) Chap. 20.

[27]K. Oura, V. G. Lifshits, A. A. Saranin, et al., *Surface science: an introduction* (Springer-Verlag, 2003).

[28]A. Tan and P. Zhang, *Organized organic molecular assemblies*, Vol. 3 (Elsevier, 2018), pp. 267–276.

[29]S. R. Wagner, R. R. Lunt, and P. Zhang, "Anisotropic crystalline organic step-flow growth on deactivated si surfaces", Phys. Rev. Lett. **110**, 086107 (2013).

[30]Y. Sun, R. Wang, and K. Liu, "Substrate induced changes in atomically thin 2-dimensional semiconductors: fundamentals, engineering, and applications", Applied Physics Reviews **4**, 011301 (2017).

[31]A. V. Kolobov, Y. Saito, P. Fons, et al., "Structural metastability in chalcogenide semiconductors: the role of chemical bonding", physica status solidi (b) **257**, 2000138 (2020).

[32]Y. Saito, S. Hatayama, W. H. Chang, et al., "Discovery of a metastable van der waals semiconductor via polymorphic crystallization of an amorphous film", Mater. Horiz. **10**, 2254–2261 (2023).

[33]J. Ravnik, I. Vaskivskyi, Y. Gerasimenko, et al., "Strain-induced metastable topological networks in laser-fabricated tas2 polytype heterostructures for nanoscale devices", ACS Applied Nano Materials **2**, 3743–3751 (2019).

[34]M. S. Sokolikova and C. Mattevi, "Direct synthesis of metastable phases of 2d transition metal dichalcogenides", Chem. Soc. Rev. **49**, 3952–3980 (2020).

[35]R. Niu, J. Li, W. Zhen, et al., "Enhanced superconductivity and critical current density due to the interaction of inse2 bonded layer in (inse2)0.12nbse2", Journal of the American Chemical Society **146**, 1244–1249 (2024).

[36]J. Dong, L. Zhang, and X. Dai, "The epitaxy of 2d materials growth", Nature Communications **11**, 5862 (2020).

[37]X. Chen, X. Zhang, M. A. Koten, et al., "Interfacial charge engineering in ferroelectric-controlled mott transistors", Advances Materials **29** (2017).

[38]S. Kezilebieke, M. Huda, and V. Vaňo, "Topological superconductivity in a van der waals heterostructure", Nature **588** (2020).

[39]Z. Zheng, Q. Ma, and Z. Bi, "Unconventional ferroelectricity in moiré heterostructures", Nature **588**, 71–76 (2020).

[40]A. Koma, "Van der waals epitaxy—a new epitaxial growth method for a highly lattice-mismatched system", Thin Solid Films **216**, 72–76 (1992).

[41]P. A. Vermeulen, J. Mulder, J. Momand, et al., "Strain engineering of van der waals heterostructures", Nanoscale **10**, 1474–1480 (2018).

[42]F. Cossu, K. Palotás, S. Sarkar, et al., "Strain-induced stripe phase in charge-ordered single layer nbse2", NPG Asia Mater **12** (2020).

[43]P. San-Jose, A. Gutiérrez-Rubio, M. Sturla, and F. Guinea, "Spontaneous strains and gap in graphene on boron nitride", Phys. Rev. B **90**, 075428 (2014).

[44]A. Summerfield, A. Davies, and T. S. Cheng, "Strain-engineered graphene grown on hexagonal boron nitride by molecular beam epitaxy", Sci Rep **1**, 22440 (2016).

[45]F. A. Rasmussen and K. S. Thygesen, "Computational 2d materials database: electronic structure of transition-metal dichalcogenides and oxides", The Journal of Physical Chemistry C **119**, 13169–13183 (2015).

[46]X. Dong, T. A. Pham, C. Xu, et al., "Growth and electronic properties of snse2 films on reconstructed, (111)-oriented srtio3 substrates", The Journal of Physical Chemistry C **127**, 16732–16739 (2023).

[47]X. Dong, W. Lai, and P. Zhang, "Semiconductor to topological insulator transition induced by stress propagation in metal dichalcogenide core–shell lateral heterostructures", Mater. Horiz. **8**, 1029–1036 (2021).

[48]S. Shabani, D. Halbertal, W. Wu, et al., "Deep moiré potentials in twisted transition metal dichalcogenide bilayers", Nature Physics **17**, 1–6 (2021).

[49]S. Behura, A. Miranda, and S. Nayak, "Moiré physics in twisted van der waals heterostructures of 2d materials", emergent mater **4**, 813–826 (2021).

[50]K. P. Nuckolls and A. Yazdani, "A microscopic perspective on moiré materials", Nature Reviews. Materials **9** (2024).

[51]C. Lu, C. J. Butler, and J. K. Huang, "Moiré-related in-gap states in a twisted mos2/graphite heterojunction", npj 2D Mater Appl **1** (2017).

[52]D. A. Ruiz-Tijerina and V. I. Falḱo, "Interlayer hybridization and moiré superlattice minibands for electrons and excitons in heterobilayers of transition-metal dichalcogenides", Phys. Rev. B **99**, 125424 (2019).

[53]Á. Rodríguez, J. Varillas, and G. Haider, "Complex strain scapes in reconstructed transition-metal dichalcogenide moiré superlattices", ACS Nano **17**, 7787–7796 (2023).

[54]K. Kang, W. Zhao, and Y. Zeng, "Switchable moiré potentials in ferroelectric wte2/wse2 superlattices", Nat Nanotechnol **18**, 861–866 (2023).

[55]C. F. Li, W. J. Zhai, Y. Q. Li, et al., "Extremely flat band in antiferroelectric bilayer α-in2se3 with large twist-angle", New Journal of Physics **23**, 083019 (2021).

[56]B. Zheng, C. Ma, D. Li, et al., "Band alignment engineering in two-dimensional lateral heterostructures", Journal of the American Chemical Society **140**, 11193–11197 (2018).

[57]J. Wang, Z. Li, and H. Chen, "Recent advances in 2d lateral heterostructures", Nano-Micro Lett. **11**, 48 (2019).

[58]R. Yang, Z. Zhang, X. Lan, et al., "Progress and challenges in the synthesis of two-dimensional lateral heterostructures", Precision Chemistry **3**, 492–515 (2025).

[59]M. A. Herman and H. Sitter, *Molecular beam epitaxy : fundamentals and current status* (Springer-Verlag, 1989).

[60]J. Tersoff and D. R. Hamann, "Theory of the scanning tunneling microscope", Physical review. B, Condensed matter **31**, 802 (1985).

[61]N. Foundation, *Press release*, Available at `https://www.nobelprize.org/prizes/physics/1986/press-release/`, 1986.

[62]C. J. Chen, *Introduction to scanning tunneling microscopy* (Oxford University Press, 1993).

[63]G. Binnig and H. Rohrer, "The scanning tunneling microscope", Scientific American **253**, 50–56 (1985).

[64]F. Bischoff, W. Auwärter, J. V. Barth, et al., "Nanoscale phase engineering of niobium diselenide", Chemistry of Materials **29**, 9907–9914 (2017).

[65]Y. Du, G. Liu, W. Ruan, et al., "Unveiling resilient superconducting fluctuations in atomically thin $NbSe_2$ through higgs mode spectroscopy", Phys. Rev. Lett. **134**, 066002 (2025).

[66]M. Ugeda, A. Bradley, and Y. Zhang, "Characterization of collective ground states in single-layer nbse2", Nature Phys **12**, 92–97 (2016).

[67]Y. Nakata, K. Sugawara, and A. Chainani, "Robust charge-density wave strengthened by electron correlations in monolayer 1t-tase2 and 1t-nbse2", Nat Commun **12**, 5873 (2021).

[68]M. Calandra, "Phonon-assisted magnetic mott-insulating state in the charge density wave phase of single-layer $1T-NbSe_2$", Phys. Rev. Lett. **121**, 026401 (2018).

[69]Z.-Y. Liu, S. Qiao, B. Huang, et al., "Charge transfer gap tuning via structural distortion in monolayer 1t-nbse2", Nano Letters **21**, 7005–7011 (2021).

[70]R. Pico, P. Abufager, I. Hamad, et al., "Understanding the interlayer coupling in $1T/1H-NbSe_2$ heterobilayers", Phys. Rev. B **110**, 075427 (2024).

[71]Z. Huang, X. Song, Y. Chen, et al., "Size dependence of charge-density-wave orders in single-layer $NbSe_2$ hetero/homophase junctions", The Journal of Physical Chemistry Letters **13**, 1901–1907 (2022).

[72]Y. Nakata, K. Sugawara, and R. Shimizu, "Monolayer $1T - NbSe_2$ as a mott insulator", NPG Asia Mater **8**, e321 (2016).

[73]F. Calavalle, P. Dreher, A. P. Surdendran, et al., "Tailoring superconductivity in large-area single-layer $NbSe_2$ via self-assembled molecular adlayers", Nano Letters **21**, 136–143 (2021).

[74]Z. Liu, H. Jin, Y. Zhang, et al., "Charge-density wave mediated quasi-one-dimensional kondo lattice in stripe-phase monolayer $1T - NbSe_2$", Nat Commun **15**, 1039 (2024).

[75]M.-X. Wang, P. Li, J.-P. Xu, et al., "Interface structure of a topological insulator/superconductor heterostructure", New Journal of Physics **16**, 123043 (2014).

[76]A. Fang, C. Adamo, S. Jia, et al., "Bursting at the seams: rippled monolayer bismuth on nbse₂", Science Advances **4**, eaaq0330 (2018).

[77]P. M. Litwin, S. T. Jaszewski, W. L. Sarney, et al., "The growth of self-intercalated $Nb_[1+x]Se_2$ by molecular beam epitaxy: the effect of processing conditions on the structure and electrical resistivity", Journal of Vacuum Science and Technology A **41**, 042707 (2023).

[78]X. Song, X. Huang, H. Yang, et al., "Robust behavior of charge density wave quantum motif star-of-david in 2d $NbSe_2$ nanocrystals", Small **19**, 2305159 (2023).

[79]E. Kamil, J. Berges, G. Schönhoff, et al., "Electronic structure of single layer $1T - NbSe_2$: interplay of lattice distortions, non-local exchange, and mott–hubbard correlations", Journal of Physics: Condensed Matter **30**, 325601 (2018).

[80]L. Liu, H. Yang, and Y. Huang, "Direct identification of mott hubbard band pattern beyond charge density wave superlattice in monolayer $1T - NbSe_2$", Nat Commun **12**, 1987 (2021).

[81]U. Chatterjee, J. Zhao, and M. Iavarone, "Emergence of coherence in the charge-density wave state of $2H - NbSe_2$", Nat Commun **6**, 6313 (2015).

[82]E. Oh, G. Gye, and H. W. Yeom, "Defect-selective charge-density-wave condensation in $2H$−$NbSe_2$", Phys. Rev. Lett. **125**, 036804 (2020).

[83]N. Balakrishnan, E. D. Steer, E. F. Smith, et al., "Epitaxial growth of γinse and α, β, and γ-in2se3 on $epsilon$-gase", 2D Materials **5**, 035026 (2018).

[84]Z. Zhang, Y. Yuan, W. Zhou, et al., "Strain-induced bandgap enhancement of inse ultrathin films with self-formed two-dimensional electron gas", ACS Nano **15**, 10700–10709 (2021).

[85]G. Han, Z.-G. Chen, J. Drennan, and J. Zou, "Indium selenides: structural characteristics, synthesis and their thermoelectric performances", Small **10**, 2747–2765 (2014).

[86]S. Lei, L. Ge, S. Najmaei, et al., "Evolution of the electronic band structure and efficient photo-detection in atomic layers of inse", ACS Nano **8**, 1263–1272 (2014).

[87]L. Debbichi, O. Eriksson, and S. Lebègue, "Two-dimensional indium selenides compounds: an

ab initio study", The Journal of Physical Chemistry Letters **6**, 3098–3103 (2015).

[88]Z. Song, X. Sun, and L. Wang, "Switchable asymmetric moiré patterns with strongly localized states", The Journal of Physical Chemistry Letters **11**, 9224–9229 (2020).

[89]Y. Sun, S. Luo, X.-G. Zhao, et al., "Inse: a two-dimensional material with strong interlayer coupling", Nanoscale **10**, 7991–7998 (2018).

[90]F. Zhang, Z. Wang, J. Dong, et al., "Atomic-scale observation of reversible thermally driven phase transformation in 2d in2se3", ACS Nano **13**, 8004–8011 (2019).

[91]M. Küpers, P. M. Konze, A. Meledin, et al., "Controlled crystal growth of indium selenide, in2se3, and the crystal structures of α-in2se3", Inorganic Chemistry **57**, 11775–11781 (2018).

[92]M. Alidoosti, D. N. Esfahani, and R. Asgari, "Charge density wave and superconducting phase in monolayer inse", Phys. Rev. B **103**, 035411 (2021).

[93]E. Stepanov, V. Harkov, M. Rösner, et al., "Coexisting charge density wave and ferromagnetic instabilities in monolayer inse", npj Comput Mater **8**, 118 (2022).

[94]A. Matetskiy, V. Mararov, N. Denisov, et al., "Characterization of the ferroelectric phase transition in monolayer in2se3 grown on bilayer graphene", Applied Surface Science **600**, 154032 (2022).

[95]H. Li, J. Luo, J. Zhang, et al., "Crystal structure and chemical bonding of layered α-in2se3", The Journal of Physical Chemistry C **127**, 22510–22517 (2023).

[96]M. Soleimani and M. Pourfath, "Ferroelectricity and phase transitions in in2se3 van der waals material", Nanoscale **12**, 22688–22697 (2020).

[97]F. Xue, W. Hu, K.-C. Lee, et al., "Room-temperature ferroelectricity in hexagonally layered α-in2se3 nanoflakes down to the monolayer limit", Advanced Functional Materials **28**, 1803738 (2018).

[98]B. Lv, Z. Yan, W. Xue, et al., "Layer-dependent ferroelectricity in 2h-stacked few-layer α-in2se3", Mater. Horiz. **8**, 1472–1480 (2021).

[99]C. Cui, W.-J. Hu, X. Yan, et al., "Intercorrelated in-plane and out-of-plane ferroelectricity in ultrathin two-dimensional layered semiconductor in2se3", Nano Letters **18**, 1253–1258 (2018).

[100]Z. Chen, W. Fu, L. Wang, et al., "Atomic imaging of electrically switchable striped domains in β-in2se3", Advanced Science **8**, 2100713 (2021).

[101]J. Zhang, X. Zhang, Y. Wang, et al., "Giant bandgap engineering in two-dimensional ferroelectric α-in2se3", The Journal of Physical Chemistry Letters **13**, 3261–3268 (2022).

[102]X. Niu, C. Pan, A. Shi, et al., "Van der waals stacking of multilayer in2se3 with 2d metals induces transition from schottky to ohmic contact", Applied Surface Science **617**, 156557 (2023).

[103]Z. Wang and W. Zhu, "Tunable band alignments in 2d ferroelectric α-in2se3 based van der waals heterostructures", ACS Applied Electronic Materials **3**, 5114–5123 (2021).

[104]F. Zhang, Z. Wang, and L. Liu, "Atomic-scale manipulation of polar domain boundaries in monolayer ferroelectric in2se3", Nat Commun **15**, 718 (2024).

[105]H. Bai, X. Wang, W. Wu, et al., "Nonvolatile ferroelectric control of topological states in two-dimensional heterostructures", Phys. Rev. B **102**, 235403 (2020).

[106]Z. Tian, Z. Zhu, J. Zeng, et al., "Ferroelectrically tunable topological phase transition in In_2Se_3 thin films", Phys. Rev. B **109**, 085432 (2024).

[107]Z. Zhang, J. Nie, Z. Zhang, et al., "Atomic visualization and switching of ferroelectric order in β-in2se3 films at the single layer limit", Advanced Materials **34**, 2106951 (2022).

[108]J. Stroscio, W. de, Phillip, C. Berger, T. Seyller, and J.-S. Moon, "Epitaxial graphenes on silicon carbide", Materials Research Bulletin (2010).

[109]R. Gong, H. Song, J. Yang, et al., "Optimization of sic cleaning process based on zeta potential", Academic Journal of Science and Technology **5**, 158–162 (2023).

[110]M. Kubo, M. Hidaka, M. Kageyama, et al., "Novel cleaning method of sic wafer with transition metal complex", Materials Science Forum **717-720**, 877, 880 (2012).

[111]M. Hupalo, E. H. Conrad, and M. C. Tringides, "Growth mechanism for epitaxial graphene on vicinal 6H-SiC(0001) surfaces: a scanning tunneling microscopy study", Phys. Rev. B **80**, 041401 (2009).

[112]K. Tamoev, M. Chugh, H. Mirhosseini, et al., "Tight binding molecular dynamics study of growth of nanostructure materials", Modelling and Simulation in Materials Science and Engineering **33**, 025001 (2025).